

Equatorial circular orbits of neutral test particles in the Kerr–Newman spacetime

Daniela Pugliese¹ and Hernando Quevedo^{2,3,4}, and Remo Ruffini^{2,2}

¹ *School of Mathematical Sciences, Queen Mary, University of London,
Mile End Road, London E1 4NS, United Kingdom*

² *Dipartimento di Fisica and ICRA, Università di Roma “La Sapienza”, Piazzale Aldo Moro 5, I-00185 Roma, Italy
ICRANet, Piazzale della Repubblica 10, I-65122 Pescara, Italy*

³ *Instituto de Ciencias Nucleares, Universidad Nacional Autónoma de México,
AP 70543, México, DF 04510, Mexico*

⁴ *Instituto de Cosmologia, Relatividade e Astrofisica and ICRANet - CBPF
Rua Dr. Xavier Sigaud, 150, CEP 22290-180, Rio de Janeiro, Brazil **

(Dated: June 19, 2018)

We present a detailed analysis of the orbital circular motion of electrically neutral test particles on the equatorial plane of the Kerr-Newman spacetime. Many details of the motion in the cases of black hole and naked singularity sources are pointed out. We identify four different types of orbital regions, which depend on the properties of the orbital angular momentum, and define four different kinds of naked singularities, according to the values of the charge-to-mass ratio of the source. It is shown that the presence of a particular type of counter-rotating test particles is sufficient to uniquely identify naked singularities. It is pointed out that the structure of the stability regions can be used to differentiate between black holes and naked singularities.

PACS numbers: 04.20.-q, 04.70.Bw, 04.40.Dg, 97.10.Gz

I. INTRODUCTION

The Kerr-Newman (KN) spacetime is an exact solution of the Einstein-Maxwell equations that describes the exterior gravitational and electromagnetic fields of a rotating charged source with mass M , angular momentum J and electric charge Q . In Boyer-Lindquist coordinates, the KN line element can be written as

$$ds^2 = -\frac{(\Delta - a^2 \sin^2 \theta)}{\Sigma} dt^2 - \frac{2a \sin^2 \theta (r^2 + a^2 - \Delta)}{\Sigma} dt d\phi + \left[\frac{(r^2 + a^2)^2 - \Delta a^2 \sin^2 \theta}{\Sigma} \right] \sin^2 \theta d\phi^2 + \frac{\Sigma}{\Delta} dr^2 + \Sigma d\theta^2, \quad (1)$$

where we used geometrized units with $G = 1 = c$, and

$$\Delta = r^2 - 2Mr + a^2 + Q^2, \quad (2)$$

and

$$\Sigma = r^2 + a^2 \cos^2 \theta. \quad (3)$$

The parameter a stands for the angular momentum per unit mass, as measured by a distant observer. The corresponding electromagnetic vector potential

$$A_\alpha = -\frac{Qr}{\Sigma} [(dt)_\alpha - a \sin^2 \theta (d\phi)_\alpha], \quad (4)$$

depends on the charge Q and the specific angular momentum a . It then follows that the magnetic field is generated by the rotation of the charge distribution.

The limiting cases of the KN metric are the Kerr metric for $Q = 0$, the Schwarzschild metric which is recovered for $a = Q = 0$, the Reissner-Nordström (RN) spacetime for $a = 0$, and the Minkowski metric of special relativity for

*Electronic address: d.pugliese.physics@gmail.com, quevedo@nucleares.unam.mx, ruffini@icra.it

$a = Q = M = 0$. The KN spacetime is asymptotically flat and free of curvature singularities outside a region situated very close to the origin of coordinates.

Several critical points characterize the geometric and physical properties of this spacetime. In particular, the function Δ vanishes at the radii

$$r_{\pm} \equiv M \pm \sqrt{M^2 - a^2 - Q^2} \quad (5)$$

which are real only if the condition $M^2 \geq Q^2 + a^2$ is satisfied. In this case, r_+ and r_- represent the radius of the outer and inner horizon, respectively, and the KN solution is interpreted as describing the exterior field of a rotating charged black hole (BH). In the case $M^2 < a^2 + Q^2$, no zeros of Δ exist and the gravitational field corresponds to that of a naked ring singularity situated at

$$r^2 + a^2 \cos^2 \theta = 0. \quad (6)$$

The norm of the timelike Killing vector field $\xi_t^\alpha = \delta_t^\alpha$ for the KN metric in Boyer-Lindquist coordinates (1) reads

$$g_{tt} = -\frac{\Delta - a^2 \sin^2 \theta}{\Sigma}, \quad (7)$$

Then, the norm is positive in the region where

$$r^2 + a^2 \cos^2 \theta + Q^2 - 2Mr < 0, \quad (8)$$

or

$$r_\epsilon^- < r < r_\epsilon^+ \quad \text{with} \quad r_\epsilon^\pm \equiv M \pm \sqrt{M^2 - Q^2 - a^2 \cos^2 \theta} \quad (9)$$

where $M^2 - Q^2 - a^2 \cos^2 \theta \geq 0$ is satisfied. In particular, for a black hole it is $r_+ < r < r_\epsilon^+$ a region which is known as the ergosphere. In the regions where ξ_t becomes spacelike, the coordinate t cannot be used as a time coordinate and the analysis of the physical properties of this spacetime requires a different approach.

The extrema of g_{tt} are located in

$$r_\pm^* = \frac{Q^2 \pm \sqrt{2a^2 M^2 + Q^4 + 2a^2 M^2 \cos(2\theta)}}{2M}, \quad (10)$$

which is a function of the parameters a and Q , and the coordinate θ . At these radii we find that

$$-g_{tt}(r_\pm^*) = \frac{2a^2 + \left(Q^2 \mp \sqrt{2a^2 M^2 + Q^4 + 2a^2 M^2 \cos(2\theta)}\right) \sec^2 \theta}{2a^2}, \quad (11)$$

so that g_{tt} has a maximum at $r = r_+^*$. The limiting cases of these radii are of interest. When $a = 0$ (Reissner-Nordström spacetime) we have

$$r_+^* = \frac{Q^2}{M}, \quad r_-^* = 0, \quad g_{tt}(r_+^*) = -1 + \frac{M^2}{Q^2}. \quad (12)$$

For a Kerr spacetime, $Q = 0$, we have that

$$r_+^* = \sqrt{a^2 \cos^2 \theta}, \quad r_-^* = -\sqrt{a^2 \cos^2 \theta}, \quad g_{tt}(r_+^*) = -\left(1 - \frac{M^2}{\sqrt{a^2 M^2 \cos^2 \theta}}\right). \quad (13)$$

In this work, we will perform a detailed analysis of the motion of test particles along circular orbits on the equatorial plane of the KN spacetime. Since test particles moving along circular orbits are particularly appropriate to measure the effects generated by naked singularities, we will focus on the study of the physical differences between a black hole and a naked singularity; see also [1–3] and for further applications [4, 5]. Although most known astrophysical compact objects possess only a small net charge or no charge at all, the study of the KN spacetime is important from the conceptual and theoretical points of view. The KN is probably the most important exact solution of the Einstein-Maxwell equations and, therefore, represents an ideal framework to study the interaction between the electromagnetic field and the gravitoelectric and gravitomagnetic components of gravity. Moreover, the detailed study of an exact solution usually sheds light on the extent of applicability of the solution and the theory itself. In this work, we study the KN solution from the point of view of the neutral circular motion, and compare our results with those obtained

in the RN and Kerr spacetimes. To this end, the spin and charge are gradually changed between the limiting cases of $a/M = 0$, $Q/M = 0$ and the KN case. We first fix the charge-to-mass ratio and let the spin change from zero to the black hole and the naked singularity regime. Then, we fix the spin and let the charge change, comparing the naked singularity and black hole spacetime properties.

This work follows a series of papers [6–8] in which we showed the presence of a typical band structure, i.e., disconnected regions of stable orbits for the spacetimes generated by Kerr and RN naked singularities. This structure is absent in the case of black holes. It was also found that there exist two types of singularities that affect the properties of the orbits and their stability. We generalize here those works considering a field source with charge and intrinsic angular momentum.

The plan of this paper is the following: In Sec. II, we introduce the effective potential for a neutral test particle moving along a circular orbit on the equatorial plane, and we set the main notations to be used in this work. In Sec. III, we explore the motion in the spacetime of a KN black hole while the case of a naked singularity is explored in Sec. IV. Section V summarizes the main results and compare the two cases. Finally, the conclusions in Sec. VI close this article.

II. CIRCULAR ORBITS

We consider the circular motion of a test particle of mass μ in the background represented by the KN metric (1). We limit ourselves to the case of orbits situated on the equatorial plane. We adopt the effective potential approach to the study of the test particle dynamics. The test particle motion is therefore described as the one-dimensional motion of a classical particle in the effective potential $V(r)$. In the case of equatorial geodesics ($\theta = \pi/2$), one obtains the effective potential [9]

$$V = -\frac{B}{2A} + \frac{\sqrt{B^2 - 4AC}}{2A}, \quad (14)$$

where

$$A \equiv (r^2 + a^2)^2 - a^2\Delta, \quad (15)$$

$$B \equiv -2aL(r^2 + a^2 - \Delta), \quad (16)$$

$$C \equiv a^2L^2 - (M^2r^2 + L^2)\Delta. \quad (17)$$

Here $L = \mu g_{\alpha\beta} \xi_\phi^\alpha u^\beta$ is a constant of motion associated with the angular momentum of the test particle with mass μ and 4-velocity u^β . The Killing vector $\xi_\phi = \partial_\phi$ represents the axial symmetry of the rotating source. The additional Killing vector $\xi_t = \partial_t$ is timelike and represents the stationarity of the field configuration. It also generates a constant of motion $E = -\mu g_{\alpha\beta} \xi_t^\alpha u^\beta$ which is associated with the total energy of the test particle, as measured by a static observer at infinity.

Notice that the effective potential (14) was obtained originally as the solution of a quadratic algebraic equation so that the solution

$$V^- = -\frac{B}{2A} - \frac{\sqrt{B^2 - 4AC}}{2A} \quad (18)$$

is also allowed. Nevertheless, this solution does not need to be analyzed separately, because its properties can be obtained from V by using the symmetry $V^-(-L) = -V(L)$.

Circular orbits are given by the simultaneous solutions of the equations

$$V = E/\mu \quad \text{and} \quad \frac{dV}{dr} = 0. \quad (19)$$

The potential (14) is quadratic in the charge Q . We therefore will limit ourselves to the study of the case $Q > 0$. Moreover, the effective potential is invariant under a simultaneous change of the sign of a and L . Consequently, without loss of generality, we can restrict the analysis to the case $a > 0$, and will differentiate between corotating particles with $L > 0$ and counter-rotating particles with $L < 0$.

To perform a detailed analysis of the effective potential of a naked singularity with $a^2 + Q^2 > M^2$, we will consider the cases

$$a > M, \quad \text{or} \quad Q > M, \quad (20)$$

otherwise

$$M > a > a_s, \quad \text{and} \quad Q < M, \quad a_s \equiv \sqrt{M^2 - Q^2}, \quad (21)$$

or

$$M > Q > Q_s, \quad \text{and} \quad a < M, \quad Q_s \equiv \sqrt{M^2 - a^2}. \quad (22)$$

For a discussion of the motion in a KN spacetime see [10–18] and also [19–21].

We introduce also the radii $r_{\pm}^{\text{RN}} \equiv r_{\pm}(a=0) = M \pm \sqrt{M^2 - Q^2}$ for the horizons of the Reissner–Nordström black hole, and $r_{\pm}^{\text{K}} \equiv r_{\pm}(Q=0) = M \pm \sqrt{M^2 - a^2}$ for the horizons of the Kerr black hole, respectively. Notice that r_{\pm}^{RN} coincides with the ergosphere boundaries r_{ϵ}^{\pm} on the equatorial plane $\theta = \pi/2$. On this plane the ergosphere is completely independent from the source spin. In particular, for a KN naked singularity there is a change of sign in the time-time component of the metric tensor (and in the norm of the timelike Killing vector) inside the region $[r_{\epsilon}^{-}, r_{\epsilon}^{+}]$, for $a \leq M$ and $Q_s < Q < M$ and $a > M$ with $Q < M$.

A. Circular motion around black holes and naked singularities

In this section, we introduce the basic equations of the circular motion in the KN spacetime, we fix the main notations and introduce the most important quantities that are relevant for the characterization of the motion both in the black hole and in the naked singularity case.

In order to explore the circular motion around black holes and naked singularities, we first study the condition $V' = 0$. Thus, we analyze the equations for the circular motion

$$V'(r, L, a, Q) = 0, \quad V = E/\mu, \quad (23)$$

and solve them with respect to the angular momentum of the test particle. We obtain that the general solution corresponds to $L = \pm L_{\pm}$, where

$$\frac{L_{\pm}}{\mu} \equiv \frac{1}{r^2} \sqrt{\frac{\Sigma \pm 2M^2 \sqrt{\Pi}}{\Psi}} \quad (24)$$

with

$$\Psi \equiv 4a^2 (Q^2 - rM) + [2Q^2 + (r - 3M)r]^2 \quad (25)$$

$$\Pi \equiv -a^2 (Q^2 - rM) r^4 [a^2 + Q^2 + (r - 2M)r]^2 [a^2 (Q^2 - Mr) + (2Q^2 - 3Mr) r^2]^2, \quad (26)$$

$$\Sigma \equiv r^2 \left\{ -(Q^2 - Mr) r^4 [2Q^2 + (r - 3M)r] + a^4 (Q^2 - Mr) [2Q^2 - (5M + r)r] + a^2 [2Q^6 + Q^4(r - 11M)r - 2Q^2(r - 2M)r^2(5M + r) + 2Mr^3[r(3M + r) - 6M^2]] \right\}. \quad (27)$$

The evaluation of the corresponding energies leads to

$$E(\pm L_{\mp}) = \frac{-(\pm L_{\mp}) (Q^2 - 2Mr) + \sqrt{r^2 [a^2 + Q^2 + (r - 2M)r] (r^2 (L_{\mp}^2 + r^2) + a^2 [r(2M + r) - Q^2])}}{r^4 + a^2 [r(2M + r) - Q^2]}. \quad (28)$$

Now, the main point is to find the regions in the space of the radial coordinate and parameters $\{r/M, Q/M, a/M\}$ where the solutions for the angular momentum and the energy are well defined. For instance, in Fig. 1, we show the behavior of the particle angular momentum and energy in the case $a = 1.1M$ for different values of the naked singularity charge Q . In Fig. 2, we present the numerical results for the case $a = 2M$ and different values of the naked singularity charge Q . First, we study the orbital regions in which circular motion occurs, that is, where solutions of Eq. (23) for L exist. These regions have as boundaries the solutions of $\Psi = 0$ or explicitly

$$r^4 - 6Mr^3 + (4Q^2 + 9M^2) r^2 - 4(3Q^2 + a^2) Mr + 4Q^4 + 4a^2 Q^2 = 0. \quad (29)$$

The solutions of Eq. (29) are the radii

$$r_{\pm}^{\pm} \equiv \frac{1}{6} \left[9M + \sqrt{3\Upsilon} \pm \sqrt{3} \sqrt{27M^2 - 24Q^2 + \frac{24\sqrt{3}Ma^2}{\sqrt{\Upsilon}} - \Upsilon} \right], \quad (30)$$

$$r_{\pm}^{\mp} \equiv \frac{1}{6} \left[9M - \sqrt{3\Upsilon} \pm \sqrt{3} \sqrt{27M^2 - 24Q^2 - \frac{24\sqrt{3}Ma^2}{\sqrt{\Upsilon}} - \Upsilon} \right],$$

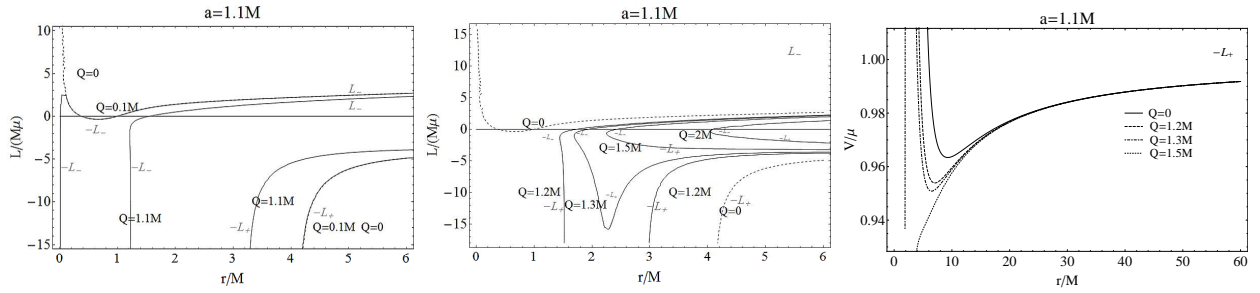


FIG. 1: The angular momentum of circular orbits is plotted as a function of the orbital radius for different source charge–mass ratio Q/M . Circular orbits in the KN spacetime with $a = 1.1M$ are explored. Right: The energy V/μ of circular orbits as a function of r/M for selected values of Q/M .

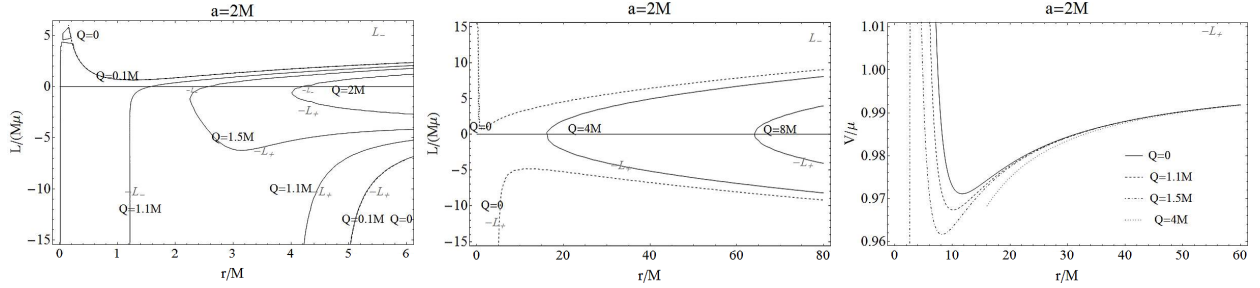


FIG. 2: Circular orbits in the KN spacetime with $a = 2M$ are explored. The angular momentum of circular orbits is plotted as a function of the orbital radius for different source charge–mass ratios Q/M . Right: The energy V/μ of circular orbits as a function of r/M for selected values of Q/M .

where

$$\begin{aligned} \Upsilon &\equiv 9M^2 - 8Q^2 + \frac{(9M^2 - 8Q^2)^2 + 24a^2(2Q^2 - 3M^2)}{\varsigma^{1/3}} + \varsigma^{1/3}, \\ \varsigma &\equiv 216M^2a^4 - (8Q^2 - 9M^2)^3 - 36a^2(27M^4 - 42M^2Q^2 + 16Q^4) + \\ &\quad 24\sqrt{3}a^2\sqrt{(Q^2 + a^2 - M^2)[27M^4a^2 - Q^2(9M^2 - 8Q^2)^2]}. \end{aligned} \quad (31)$$

The study of the regions confined by these radii will be the key point to analyze the circular orbits of neutral particles in a KN naked singularity and to distinguish this case from the black hole one.

We see that in general there are four possible different radii and all of them depend on the value of the parameters M , Q and a that characterize the rotating source. For a given value of the source parameters not all the solutions lead to real and positive radii so that many different cases can arise. For a better presentation of the results it is convenient to introduce the notation

$$r_1 \equiv r_-, \quad r_2 \equiv r_+, \quad r_3 \equiv r_-^+, \quad r_4 \equiv r_+^+. \quad (32)$$

The behavior of these radii is illustrated in Fig. (3). Notice that in general $r_1 < r_2 < r_3 < r_4$. The existence of the surfaces is studied in detail in Fig. 4. The shaded regions contain all the points at which Eq. (29) does not possess real positive solutions. In the light gray regions of Fig. 4, four solutions exist, and in the white regions only certain radii, as indicated in the plots. Thus, to analyze these regions in detail, it is convenient to introduce the following charges

$$Q_4/M \equiv \sqrt{\frac{3}{2} \text{Sin} \left[\frac{1}{6} \arccos \left[1 - 4 \frac{a^2}{M^2} \right] \right]^2}, \quad Q_5/M \equiv \sqrt{\frac{3}{4} \left(1 + \text{Sin} \left[\frac{1}{3} \arcsin \left[1 - 4 \frac{a^2}{M^2} \right] \right] \right)}, \quad (33)$$

$$Q_6/M \equiv \sqrt{\frac{3}{2} \cos \left[\frac{1}{6} \arccos \left[-1 + 4 \frac{a^2}{M^2} \right] \right]^2}. \quad (34)$$

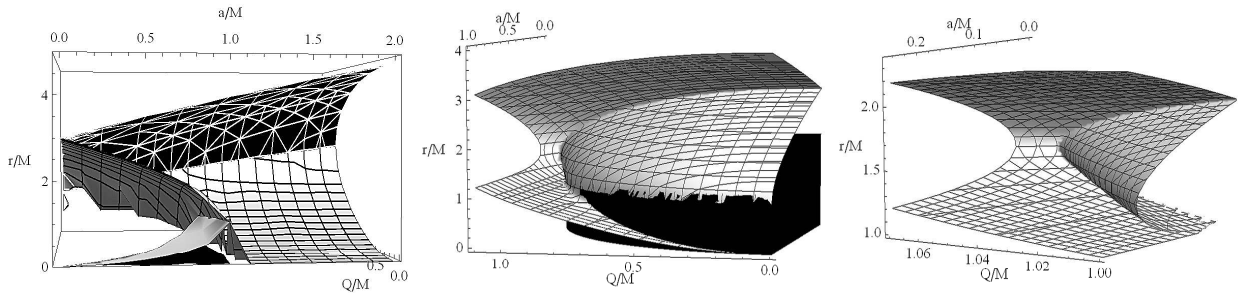


FIG. 3: Left: The radii r_1 (black surface), r_2 (white surface), r_3 (gray, black-shaded, surface), and r_4 (black, white-shaded surface) plotted as functions of $Q/M \in (0, 2)$ and $a/M \in (0, 2)$; it is $r_1 < r_2 < r_3 < r_4$. Center: Surfaces (r_1, r_2, r_3, r_4) in the the region $Q/M \in \{0, 1.1\}$, $a/M \in \{0, 1\}$, $r/M \in \{0, 4\}$. The black region represents $r < r_+$, where r_+ is the outer horizon of the black hole. Right: The region $Q/M \in \{1, 1.07\}$, $a/M \in \{0, .251\}$, $r/M \in \{1, 2.35683\}$ corresponds to the case of a naked singularity.

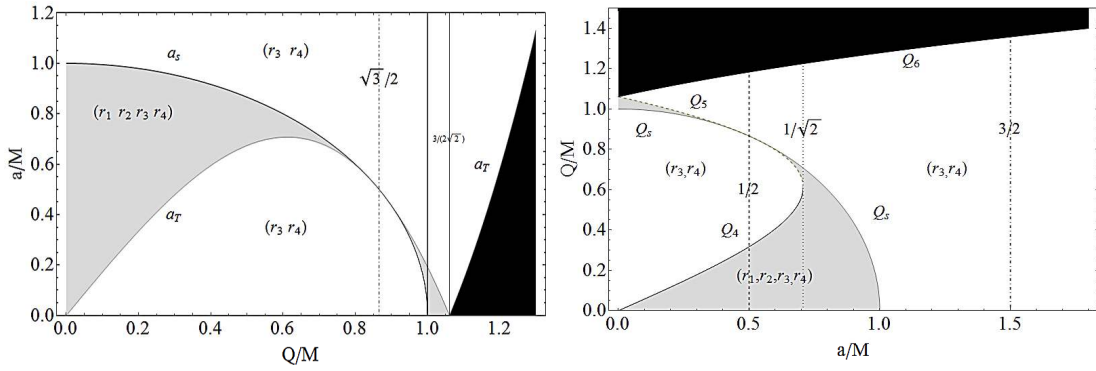


FIG. 4: Left: Plot of a_T and a_s as a function of Q/M . Right: Plot of Q_4 (black curve), Q_s (gray curve), Q_5 (dashed curve), Q_6 (black thick curve) as functions of a/M . Black regions are forbidden: no solution of Eq. (29) exists. In the white regions, Eq. (29) is satisfied for $r = r_1$, $r = r_2$, $r = r_3$ and $r = r_4$. In particular, for $Q = 0$ and $a = 0$ the solution is $r = 3M$, for $0 < a < M$ it is $r = r_2$, $r = r_3$ and $r = r_4$. For $a = M$ it is $r = M$ and $r = 4M$, finally for $a > M$ it is $r = r_3 = r_4$.

and the following spin parameter

$$a_T \equiv \frac{\sqrt{Q^2 (8Q^2 - 9M^2)^2}}{3\sqrt{3}M} \quad (35)$$

which guarantees that ζ in Eq. (30) is real.

Alternatively, it is also possible to investigate the solutions of the equation $\Psi = 0$ in terms of the source charge as a function of (a, r) . In this way we will have a different view of the regions of existence of circular orbits. Thus, the solution of $\Psi = 0$ is

$$Q_{\mp}^{\pm} \equiv \sqrt{\frac{1}{2} \left[(3M - r)M - a^2 \frac{r}{M} \pm \sqrt{a^2 (a^2 + 2(r - M)r)} \right]}, \quad (36)$$

The corresponding surfaces are studied in detail the left plot of Figs. 5, which also includes the regions where these charges exist. It is convenient to introduce the following spin parameter

$$a_{r_1} \equiv \sqrt{2r(M - r)}, \quad a_{r_2} \equiv \frac{1}{2} \sqrt{(r - 3M)^2 r / M}, \quad (37)$$

and the radii

$$r_{M\pm} \equiv \frac{1}{2} \left(M \pm \frac{1}{2} \sqrt{M^2 - 2a^2} \right), \quad (38)$$

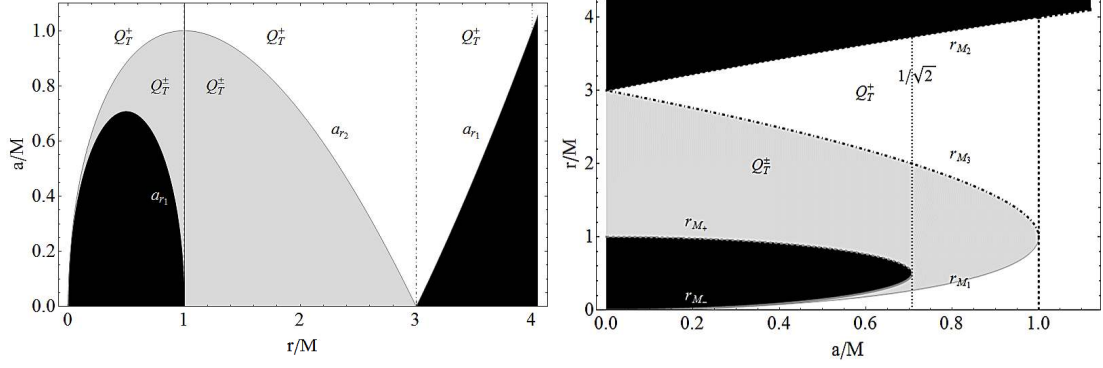


FIG. 5: Black regions are forbidden: no solution of Eq. (29) exists. Left: Plot of a_{r_1} and a_{r_2} as functions of r/M . The solutions Q_T^\pm are shown in the light-gray region and Q_T^\pm in the white regions. Right: Plot of r_{M_1} (gray curve), r_{M_2} (dashed black curve), r_{M_3} (dotted-dashed black curve), r_{M_-} (gray curve), r_{M_+} (gray dashed curve) as functions of a/M . Black regions are forbidden: no solution of Eq. (29) exists. In the white regions, the solution is $Q = Q_T^\pm$; in the light gray regions the solutions are $Q = Q_T^\mp$

which define the region $r \in]r_{M_-}, r_{M_+}[$ where no solution of Eq. (29) exists (see the right panel of Fig. 5-right). The radii

$$r_{M_1}/M \equiv 4 \sin \left[\frac{1}{6} \arccos (1 - 2a^2/M^2) \right]^2, \quad r_{M_2}/M \equiv 4 \cos \left[\frac{1}{6} \arccos (2a^2/M^2 - 1) \right]^2, \quad (39)$$

$$r_{M_3}/M \equiv 2 \left(1 + \sin \left[\frac{1}{3} \arcsin (1 - 2a^2/M^2) \right] \right), \quad (40)$$

were introduced in [7], with a different notation, in order to study the existence of circular orbits in the Kerr spacetime.

In Figs. 6, we show the solution of the equation $\Psi = 0$ in terms of the spin parameter a_i

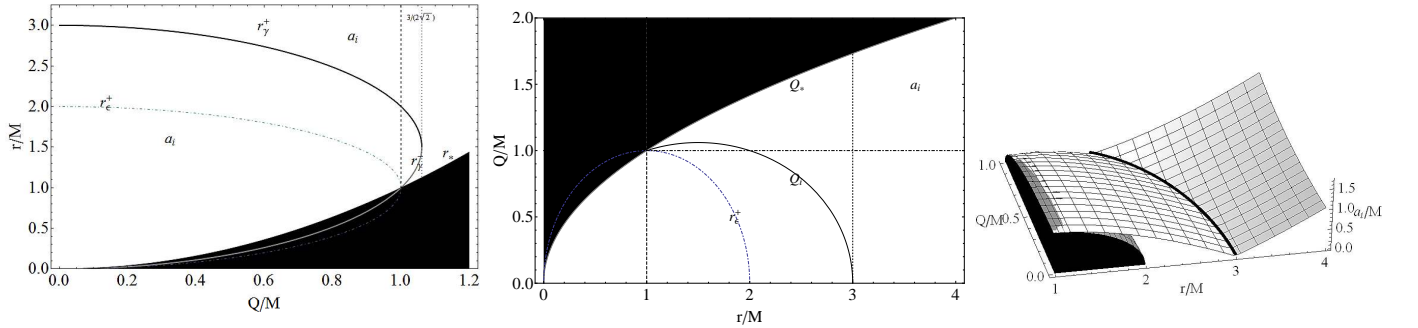


FIG. 6: Left: Plot of r_γ^+ (thick black curve), r_γ^- (thick gray curve), r_* (black curve), r_e (dotted-dashed curve) as functions of Q/M . The solution of Eq. (29) is a_i in the white regions. Center: Plot of Q_i and $Q_*/M = \sqrt{r/M}$ as functions of the radius r/M . Dotted-dashed curve signs r_e . In the white regions, Eq. (29) is satisfied for $a = a_i$. The plot is therefore divided in the regions: $0 < r < M$, $M < r \leq 3M$, $r > 3M$. In particular, at $r = M$ and $Q = 1$, a solution exists for $a \geq 0$. The dotted-dashed line is $Q = M$, the dashed line is $r = M$ and the dotted line is $r = 3M$. Right: The black hole angular momentum a_i is plotted as a function of r/M , and the charge-to-mass ratio Q/M of the black hole. The outer horizon plane r_+ (gray) is also plotted. The black region is $r < r_+$. The curve $r = r_\gamma^+$ (black thick) is also plotted.

$$a_i \equiv \frac{1}{2} \sqrt{\frac{[2Q^2 + (r - 3M)r]^2}{Mr - Q^2}}, \quad (41)$$

where we used the definitions

$$r_\gamma^\pm \equiv \frac{1}{2} \left(3M \pm \sqrt{9M^2 - 8Q^2} \right), \quad r_* \equiv Q^2/M, \quad (42)$$

and $Q_i/M \equiv \sqrt{\frac{(3M-r)r}{2M}}$ and with $Q_*/M \equiv \sqrt{r/M}$ (that corresponds to the definition $r_* = Q^2/M$). The radii (r_γ^\pm, r_*) , introduced in [6], characterize the dynamics around a Reissner-Nordström naked singularity ($Q/M > 1$) where the following inequality holds $r_* < r_\gamma^- < r_\gamma^+$, and r_γ^\pm are the radii at which the value of the angular momentum and the energy of the test particle diverge. At the classical radius r_* circular orbits exist with “zero” angular momentum. This means that a static observer situated at infinity would interpret this situation as a test particle that remains motionless as time passes. This phenomena can take place only in the case of a naked singularity and is interpreted as a consequence of the “repulsive” force generated by the charge distribution. It is interesting to note that these radii have an important role even in the presence of a non zero source spin. In particular, it turns out that from Eq. (24) the orbital angular momentum L is defined when $\Pi \geq 0$, and from Eq. (26) we recover $r \geq r_*$, at $r = r_*$ it is $L_\pm = \mu M \sqrt{\frac{M^2 a^2}{Q^2(Q^2 - M^2)}}$, which is in fact zero in the Reissner-Nordström case. In Fig. 6, we plot the behavior of these radii as functions of the ratio Q/M and a/M .

Now, for the existence of solutions of the Eq. (23) it is however necessary to demand that the solution (24) be real. Therefore, we study the solutions of the equation $\Sigma^2 - 4M^4\Pi = 0$, that is $L = 0$, or

$$-Q^4 a^2 - Q^2 a^4 + (4Q^2 a^2 + a^4)Mr - 2(2M^2 + Q^2)a^2 r^2 + 2Ma^2 r^3 - Q^2 r^4 + Mr^5 = 0, \quad (43)$$

which will be denoted by \tilde{r} (see Fig. 7). But in general we can also find the regions of circular motion by fixing the value of the source angular momentum a and plotting the ratio Q/M in terms of the radial coordinate. Thus, we can also express the solution of Eq. (43) in terms of the charge Q_c

$$Q_c \equiv \sqrt{\frac{-a^4 + a^2 \left(-2(r-2M)r + \sqrt{a^4 + 2a^2(r-2M)r + r^4} \right) + r^2 \left(-r^2 + \sqrt{a^4 + 2a^2(r-2M)r + r^4} \right)}{2a^2}}. \quad (44)$$

In this case, it is convenient to introduce the charge

$$Q_r \equiv \sqrt{-a^2 - (r-2M)r}, \quad (45)$$

which is the solution of the equation $\Delta = 0$, and the radius r_x which represents the real solutions of Eq. (43) when

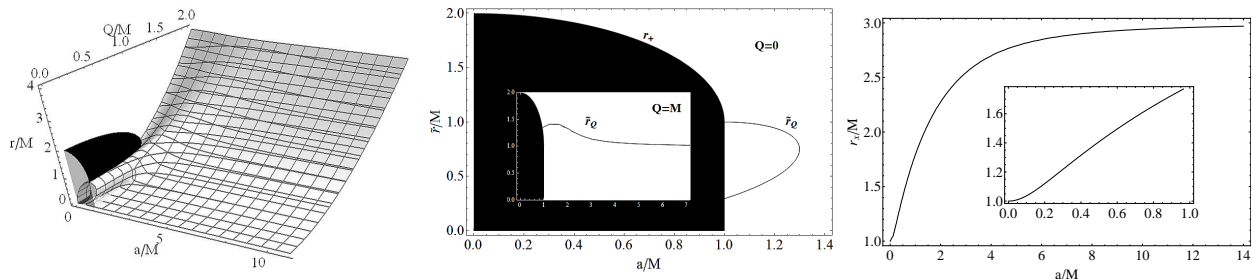


FIG. 7: Left: Plots of \tilde{r} as functions of Q/M and a/M . The surfaces $r = r_+$ and $r = r_-$, delimited by the outer and inner horizon respectively are also plotted. The region $r < r_+$ is shaded. Center: Plot of \tilde{r}_Q , that is \tilde{r} in the case $Q = 0$ and $Q = M$ (inset plot). Right: Plot of r_x in the range $[0, 3M]$ as a function of a/M . The inset plot shows a zoom for $a \leq M$.

the source charge is $Q_{\tilde{r}}^\pm$, or

$$-12Ma^4 + a^2(4a^2 - M^2)r - 12Ma^2r^2 + 5a^2r^3 - 2Mr^4 + 2r^5 = 0. \quad (46)$$

This radius is plotted in Fig. 7 for different values of the ratio a/M . Notice in particular that r_x does not depend on the source charge but only on its angular momentum.

III. BLACK HOLES

In this section, we study the Kerr–Newman black hole case, considering the constraint $\delta \geq 0$, where $\delta \equiv M^2 - Q^2 - a^2$. In particular it is $\delta = 0$ for $Q^2 + a^2 = M^2$, and $Q \in [0, M]$ and $a \in [0, M]$. For $Q = a = 0$, Schwarzschild black hole, it is $\delta = M$. In Fig. 8, the outer r_+ and inner r_- horizon surfaces are plotted as function of a/M and Q/M . We are interested in the solutions of Eq. (23) in the region $r > r_+$. Solving Eq. (23) for the angular momentum L , we obtain

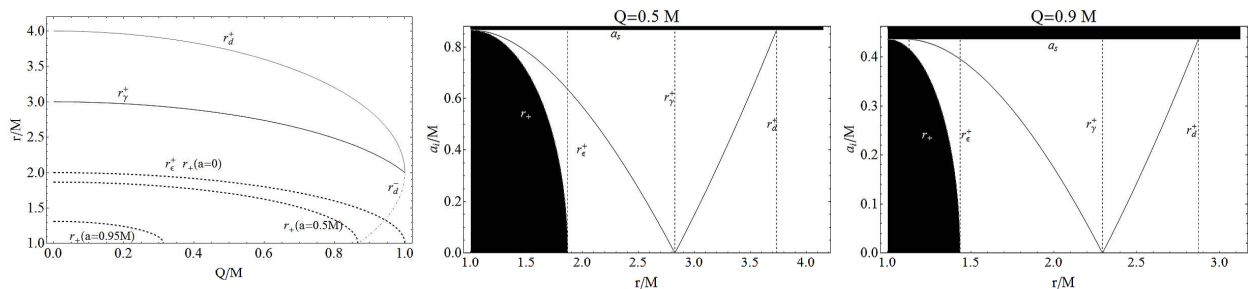


FIG. 8: Left: The outer horizon $r_+ = M + \sqrt{M^2 - a^2 - Q^2}$, the outer ergosphere radius on the equatorial plane $r_e^+ = M + \sqrt{M^2 - Q^2}$ and the radius $r_d^+ = 2r_e^+$, are plotted as functions of the black hole charge-to-mass ratio Q/M , for different values of the intrinsic angular momentum a/M . Center and Right: The outer horizon $r_+ = M + \sqrt{M^2 - a^2 - Q^2}$, the outer ergosphere radius on the equatorial plane $r_e^+ = M + \sqrt{M^2 - Q^2}$ and the radius $r_d^+ = 2r_e^+$ are plotted as functions of r/M and the black hole charge-to-mass ratio Q/M . The angular momentum $a_s = \sqrt{M^2 - Q^2}$ is plotted (gray curve); for the black hole case it is $a < a_s$. Center: $Q = 0.5M$, $a_s = 0.866M$, $r_e^+ = 1.866M$, $r_d^+ = 3.732M$, $r_d^- = 0.268M$. Right: $Q = 0.9M$, $a_s = 0.436M$, $r_e^+ = 1.436M$, $r_d^+ = 2.872M$, $r_d^- = 1.1282M$. Shaded regions are forbidden: the horizon constraint of the KN black hole implies $0 \leq a \leq a_s \leq 1$ and $r > r_+$.

the solutions given in Eq. (24). There are zones in which two kinds of orbits, characterized by two different angular momentum, but same orbital radius, are possible. In particular, it is possible to show that there are no circular orbits in the KN black hole spacetime with zero angular momentum, i. e., there are no solutions of the following equations

$$V'(r, Q, a, L) = 0, \quad L = 0. \quad (47)$$

However, one can see that $V'(r, Q, a, L = 0) > 0$ in the region $r > r_+$; this means that for particle with an “angular momentum” $L = 0$ the effective potential monotonically increases as the outer regions of spacetime are approached.

But before we deal with the general case $a \neq 0$ and $Q \neq 0$, it is useful to summarize briefly the known outcomes for the two limiting cases of Kerr ($Q = 0$) and RN ($a = 0$) spacetimes. We refer for details to the extensive literature on the subject and to the aforementioned works [6–8]. In fact, we will see that the source spin and the charge deform the regions of circular motion and the stability properties of a RN and Kerr spacetime, respectively. To discuss the dynamics of a black hole spacetime, it is convenient to introduce here the following radius

$$r_d^\pm = 2(M \pm \sqrt{M^2 - Q^2}). \quad (48)$$

We notice that $r_d^\pm = 2r_\pm^{\text{RN}}$ and, for circular motion on the equatorial plane ($\theta = \pi/2$), it is $r_d^\pm = 2r_\pm^{\text{RN}} = 2r_e^\pm$, see Figs. 8. Furthermore, it is possible to prove that the following limits are satisfied:

$$r_{M3} = r_3, \quad \text{for } Q = 0 \quad (\text{Kerr metric}), \quad (49)$$

$$r_\gamma^+ = r_3 = r_4, \quad \text{for } a = 0 \quad (\text{Reissner-Nordström metric}). \quad (50)$$

Moreover, following the notation of [7], we define the radius $r_a \equiv r_4$ ($Q = 0$), i. e.,

$$r_a \equiv 4M \cos \left[\frac{1}{6} \arccos \left[2 \frac{a^2}{M^2} - 1 \right] \right]^2. \quad (51)$$

Tables I and II show the case $Q = 0$ from two different points of view. This differentiation in the presentation of the orbital regions is important for the study of the stability problem also in the general case of a KN spacetime. In Table I, we consider different values for the source angular momentum a , ranging from the Schwarzschild black hole, $a = 0$, to the extreme Kerr black hole with $a = M$. Each range is then divided in various spatial regions, each of which is characterized by a particular value of the orbital angular momentum L of the test particle.

In Table II, we present an alternative classification of the circular orbits. The radial coordinate is split into various regions that range from $r = M$ to $r \rightarrow \infty$. It turns out that the radii $r = 3M$ and $r = 4M$ are of particular interest because they determine spatial boundaries in which the value of the orbital angular momentum L drastically depends on the source angular momentum a . In each spatial region, we present the type of allowed circular orbits (rotating and counter-rotating) with the corresponding value of the angular momentum of the test particle (L_\pm). More details about this classification can be found in [6, 7]. Finally, in the limiting case of a RN black hole ($a = 0$), one can see that circular orbits with $L = \pm L_-$ are allowed only in the region outside the radius r_γ^+ .

The main question now is to determine how the electric charge of the gravitational source will affect this classification. Since the charge generates its own gravitational field, it is expected that its presence will modify the spatial regions as well as the ranges of the source angular momentum in which circular motion can take place.

TABLE I: Angular momentum of circular orbits L in the region $r > M$ of a Kerr spacetime for specific values of the source angular momentum a .

Case: $Q = 0$ (Kerr)					
$a = 0$	(Schwarzschild)	$0 < a < M$	(Kerr)	$a = M$	(extreme Kerr)
Region	L	Region	L	Region	L
$r > 3M$	$\pm L_-$	$]r_{M_3}, r_a]$	L_-	$]M, 4M]$	L_-
		$]r_a, \infty[$	$(L_-, -L_+)$	$]4M, \infty[$	$(L_-, -L_+)$

TABLE II: Angular momentum L of circular orbits in the region $r > M$ of a Kerr spacetime for specific values of the radial coordinate r .

Case: $Q = 0$ (Kerr)							
$M < r \leq 3M$		$3M < r < 4M$		$r = 4M$		$r > 4M$	
a	L	a	L	a	L	a	L
$]a_i, M]$	L_-	$[0, a_i[$	$(L_-, -L_+)$	$[0, M[$	$(L_-, -L_+)$	$[0, M]$	$(L_-, -L_+)$
		$]a_i, M]$	L_-	M	$13/(4\sqrt{2})M\mu$		

A. Orbital regions around a KN black hole

We give here a description of circular orbits with $L \neq 0$ around a KN black hole from the outer horizon r_+ to infinity. Since it is always $r_+ > M$, in order to simplify the exploration of the dynamics in the region $r > r_+$, we approach the more general problem of finding the extremes of the effective potential in the larger region $r > M$ with the constraints $0 \leq a \leq a_s$ and $0 \leq Q \leq M$. The results of this analysis are summarized in Tables III and IV. Notice that the spin parameter $a = a_s$ plays an important role for the definition of the different ranges of Table. III, because for $Q > M$ a black hole case occurs if the source spin satisfies the condition $a \leq a_s$. We point out that there are two different orbital regions, namely, the region **I**, with $L = L_-$, and the region **II**, with $L = (L_-, -L_+)$. Table III shows the allowed angular momenta of the test particle (L), depending on the values of source spin (a), for fixed ranges of the charge Q/M and different orbital regions defined by r/M . We also include in this table the particular case of an extreme RN black hole, $Q = M$ and $a = 0$. This is a generalization of the Table II for the case $Q \neq 0$. We can see that the regions in which circular motion is allowed do not differ qualitatively from the configuration shown in Tab. II for the case $Q = 0$ in which the limits $r_\gamma^+ = 3M$ and $r_d^+ = 4M$ hold. We conclude that the introduction of a source charge does not change qualitatively the structure of the orbital regions, but only their extensions, i.e., the boundaries become modified as shown in Table III.

The extensions of the orbital regions **I** and **II** will depend on a/M and Q/M but, at least for the characteristic values of black hole spacetimes, we do not see the appearance of an additional type of orbit. For example, there are no counter-rotating orbits with $L = -L_-$ in $r > r_+$ as in the limiting case $a = 0$.

TABLE III: Description of the circular orbits for a test particle in a Kerr–Newman black hole with $0 < Q \leq M$, in the region $r > M$. The orbital angular momentum is given for each region. This is a generalization of Table II to the case $Q \neq 0$.

Case: $0 < Q \leq \sqrt{3}M/2$ ($\sqrt{3}M/2 < Q < M$)							
$(r_d^-)M < r \leq r_\gamma^+$		$r_\gamma^+ < r < r_d^+$		$r = r_d^+$		$r > r_d^+$	
a	L	a	L	a	L	a	L
$]a_i, a_s]$	L_-	$[0, a_i[$	$(L_-, -L_+)$	$[0, a_s[$	$(L_-, -L_+)$	$[0, a_s]$	$(L_-, -L_+)$
		$]a_i, a_s]$	L_-	a_s	L_-		
Case: $Q = M$							
$r > 2M$							
a	L						
$a = 0$	$\pm L_-$						

The results presented in Table III are illustrated in Figs. 9 and 10.

On the other hand, Table IV shows, for different intervals of the specific charge Q/M , the regions of existence of circular orbits for different ranges of the source spin a . For this analysis, it is convenient to define the following angular momentum parameters

$$\tilde{a}_\pm \equiv \sqrt{\frac{Q^4 - 2r(r - 2M)(rM \mp Q^2) + (2rM \mp Q^2)\sqrt{Q^4 + 4Q^2M(r - M)r - 4(r - M)Mr^2}}{2(rM - Q^2)}}, \quad (52)$$

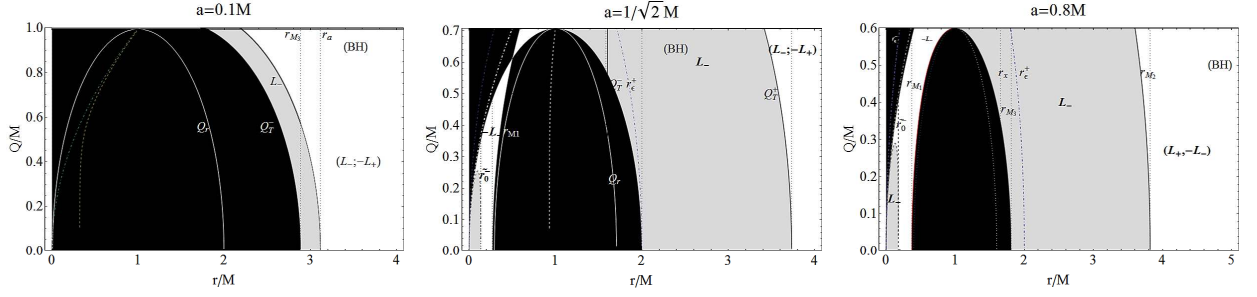


FIG. 9: Black hole case: circular orbital regions in the plane $(Q/M, r/M)$ for fixed values of a/M . The angular momentum of the orbiting test particle is shown in each spatial region. The curves Q_{T}^{\pm}/M , Q_*/M are also plotted. See also Table III. The horizons r_{\pm} are represented as white curves. The dotted-dashed curve is the outer ergosphere r_{ϵ}^+ .

TABLE IV: Description of the circular orbits for a test particle in a Kerr–Newman black hole with $0 \leq Q \leq M$, in the region $r > M$. The orbital angular momentum is given for different values of the black hole spin a/M . This is a generalization of Table I to the case $Q \neq 0$.

Case: $0 < Q < M$					
$a = 0$	(Reissner Nordström)	$0 < a < a_s$		$a = a_s$	
Region	L	Region	L	Region	L
$r > r_{\gamma}^+$	$(L_-, -L_+)$	$]r_3, r_4[$	L_-	$]r_3, r_4[$	L_-
		$]r_4, \infty[$	$(L_-, -L_+)$	$]r_4, \infty[$	$(L_-, -L_+)$
Case: $Q = M$					
$a = 0$	(Reissner Nordström)				
Region	L				
$r > 2M$	$(\pm L_-)$				

which determine the boundaries of the different regions. In the limiting case $\tilde{a}_+ = \tilde{a}_-$, these regions reduce and very particular orbits appear which are studied in detail in Appendix A.

The orbital region boundaries are determined by the radii r_{γ}^+ , r_3 and r_4 , which for fixed Q/M are in general functions of a/M . The results of Table IV are illustrated in Figs. 10.

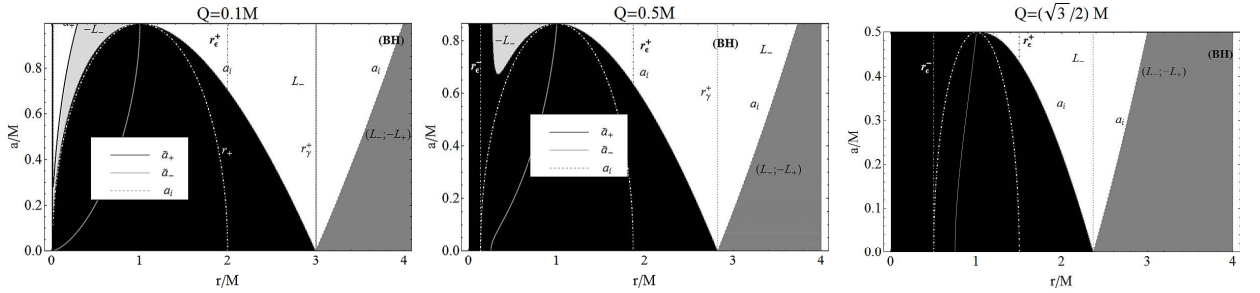


FIG. 10: Black hole case: circular orbital regions in the plane $(a/M, r/M)$ for fixed Q/M . The angular momentum of the orbiting test particle is shown in each spatial region. The intrinsic KN angular momentum \tilde{a}_-/M (gray curve), \tilde{a}_+/M (black curve) and a_i/M (dashed gray curve) are also plotted as functions of r/M . The horizons r_{\pm} are represented as white curves. See also Table IV. The dotted-dashed line is the outer ergosphere r_{ϵ}^+ .

Finally, we notice that in Figs. 9 and 10 we have represented the entire orbital range $r > 0$, although for the study of circular orbits we are restricting ourselves to the physical region outside the outer horizon $r > r_+$. Nevertheless, it is interesting to mention that, according to Figs. 9 and 10, there exist circular orbits with $L = -L_-$ in the region $r < r_-$. The study of this motion inside the inner horizon is outside the scope of the present work.

B. Stability of circular orbits

The radius of the last stable circular orbit for a neutral particle orbiting on the equatorial plane of a KN black hole is defined as the solution of the following equations:

$$V(r_{lSCO}) = E, \quad V'(r_{lSCO}) = 0, \quad V''(r_{lSCO}) = 0, \quad \text{with} \quad Q^2 + a^2 \leq M^2. \quad (53)$$

Stable (unstable) orbits are characterized by the condition $V''(r_{lSCO}) > 0$ ($V''(r_{lSCO}) < 0$). In Fig. 11, we plot r_{lSCO} as a function of the intrinsic angular momentum a and the charge Q . We note that the radius r_{lSCO} is given as a surface that has as a limiting case the planes identified by the radii r_{lSCO}^{RN} , the last stable orbit for $a = 0$, and $r_{lSCO}^{K\mp}$, the last stable orbit for $Q = 0$. The exact expressions for these radii were given in [7] and [6], respectively. We can see from Fig. 11 that the surface contained between the two limiting cases is reduced to a curve if the condition $r_{lSCO}^{RN} = r_{lSCO}^{K-}$ is satisfied. This happens when Q and a are linked by the following relation

$$Q = Q_K \equiv \frac{r_{lSCO}^{K-}}{8M} \left[9M - \sqrt{16r_{lSCO}^{K-} - 15M} \right]. \quad (54)$$

In particular, if $a = 0$, we obtain that $4M \leq r_{lSCO} \leq 6M$ and if $0 < a < M$, then the last stable orbit in the spacetime of a KN black hole is located within the bounded region $r_\beta \leq r_{lSCO} \leq 6M$ where

$$r_\beta/M \equiv \frac{3a^2 + \left(M^2 + \left[M^6 + a^2 M^2 (5M^2 + 2a^2) + \sqrt{a^2 (a^2 - M^2)^2 (M^2 + 4a^2)} \right]^{1/3} \right)^2}{\left[M^6 + a^2 M^2 (5M^2 + 2a^2) + \sqrt{a^2 (a^2 - M^2)^2 (M^2 + 4a^2)} \right]^{1/3}}. \quad (55)$$

This behavior is depicted in Fig. 11. It is interesting to mention the identity $r_\beta = r_{lSCO}^{RN}(Q = a_s)$, which means that at the boundary r_β the effective intrinsic angular momentum $\sqrt{1 - (a/M)^2}$ plays the role of the specific charge Q/M . Moreover, for the particular value $a = 0.430075M$ we obtain that $r_\beta = r_{lSCO}^{K-}$. See Fig. 11. Finally, for $a = 0$

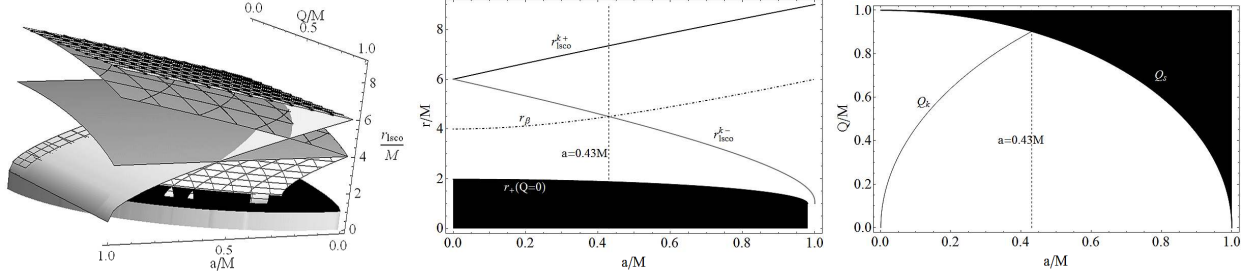


FIG. 11: Left: The outer horizon (black surface), r_{lSCO}^{RN} (gray surface), r_{lSCO}^{K-} (light-gray surface), r_{lSCO}^{K+} (white-black-thick-mashed surface), the surface $r_{lSCO}(L_-)$ (light-gray, meshed surface) and $r_{lSCO}(-L_+)$ (gray surface with black thick mash). Note that $r_{lSCO}^{K+} = r_{lSCO}^{K-}$ at $r = 6M$ and $r_{lSCO}^{K-} = r_{lSCO}^{RN}$ along the curve $Q = Q_K$ (see text) and $r_{lSCO}(-L_+) < r_{lSCO}(L_-)$. Center: Last stable circular orbit radius r_{lSCO} for a Kerr black hole ($Q = 0$) – r_{lSCO}^{K-} (gray curve) and r_{lSCO}^{K+} (black curve) –, the outer horizon r_+ , and the radius r_β (dotted-dashed curve) are plotted as functions of the KN black hole spin a/M . The dashed line represents $a = 0.430075M$. Right: The charge Q_K (black curve) of a KN black hole is plotted as a function of the momentum a/M , where $r_{lSCO}^{RN} = r_{lSCO}^{K-}$ (see text). A naked singularity exists in the region $Q > Q_s$.

and $Q = 0$ we have that $r_{lSCO} = 6M$.

In particular, we note that $E(-L_+) > E(L_-)$ in the regions where both of them are allowed. As a function of the radial coordinate, the energy of circular orbits shows points of minimum values, i.e., stable orbits. There are also radii (r_3 and r_4) at which the energy necessary for a test particle to remain in orbit around the source becomes infinite. This kind of circular orbits is also found in the RN and Kerr spacetimes.

The stability of these orbits can be studied by comparison with the Kerr black hole case. In Fig. 12, the results are shown for black holes with different charges. Following [7], we define two different radii for the last stable circular orbits as follows

$$r_{lSCO}^+ \equiv r_{lSCO}(-L_+), \quad r_{lSCO}^- \equiv r_{lSCO}(L_-) \quad (56)$$

for the orbits with angular momentum $L = -L_+$ and $L = L_-$, respectively. We now compare the general configuration for different values of $Q/M \neq 0$ with the configuration in the case of a Kerr black hole ($Q = 0$). We show in Fig. 12 that for a KN black hole the orbital regions of stability are qualitatively similar to those of a Kerr black hole [7]. The main feature is that if the charge-to-mass ratio increases, for fixed black hole spin a/M , the radius of the last stable circular orbit r_{lsc}^\pm decreases. In particular, the plots of Fig. 12 show that, for fixed a/M and for different values of

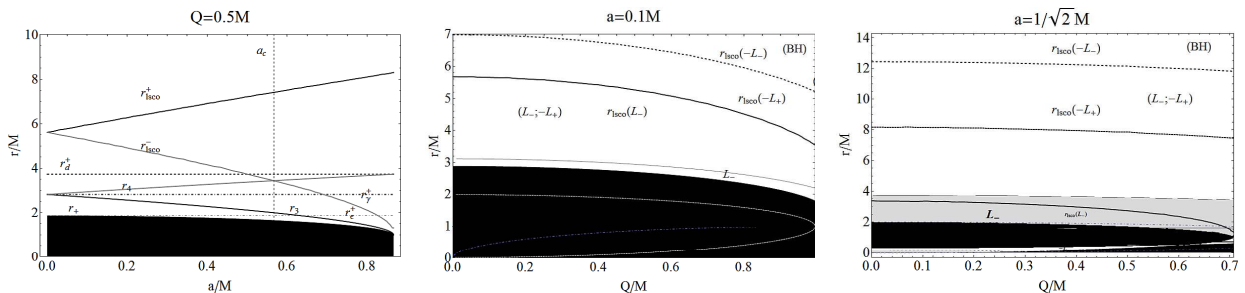


FIG. 12: Left: The radius $r_{lsc}^+ \equiv r_{lsc}(-L_+)$ and $r_{lsc}^- \equiv r_{lsc}(L_-)$ of the last stable circular orbits for a KN black hole, with fixed charge-to-mass ratio Q/M , as a function of the black hole spin $0 \leq a \leq a_s$. The horizon r_+ , the radius r_+^+ (dotted line), r_d^+ (dashed line), r_3 (black curve), r_4 (gray curve) are also plotted. The black region ($r < r_+$) is forbidden. The value of a_c , the crossing point between r_3 and r_{lsc}^- , is represented by a dashed line. The dotted-dashed line is the outer ergosphere r_e^+ . Center and Right: Last stable circular orbits $r_{lsc}(L_-)$ (thick black curve), $r_{lsc}(-L_-)$ (thick black dashed curve) and $r_{lsc}(-L_+)$ (thick black dotted curve) as functions of Q/M , for increasing values of the source spin. The angular momentum of an orbiting test particle is shown in each region. Black regions are forbidden. In the region $r < r_{lsc}$ ($r > r_{lsc}$), circular orbits are unstable (stable). The curves $L = -L_-$ exist in a region located in $r < r_-$.

Q/M , the stability regions bounded by $r_{lsc}(-L_+)$ and $r_{lsc}(L_-)$ are connected regions. This is the main result of this section and it will be important when comparing with the case of naked singularities. We can clarify the arrangement of the stability regions in a schematic way: In the region $r_+ < r < r_{lsc}(L_-)$ all orbits are unstable, in the region $r_{lsc}(L_-) < r < r_{lsc}(-L_+)$ the orbits with L_- are stable while the orbits with $L = -L_+$ are unstable, and finally in the region $r > r_{lsc}(-L_+)$ all orbits are stable. This scheme does not change significantly when the parameters Q/M and a/M are changed; however, we note that the radius $r_{lsc}(L_-)$ can lie on the right of the region I so that all the orbits with $L = L_-$ are unstable. This occurs for values of a/M sufficiently small. As a/M increases, the radius $r_{lsc}(L_-)$ becomes smaller and approaches the horizon, reducing in this way the regions of instability for the orbits $L = L_-$ which belong to both the I and II regions (see Fig. 12-left). Furthermore, the radius $r_{lsc}(L_-)$ splits the region I into two different stability zones: Orbits with $r > r_{lsc}(L_-)$ are stable whereas orbits with $r < r_{lsc}(L_-)$ are unstable (see Fig. 12-Right).

IV. NAKED SINGULARITIES

A. Orbits with zero angular momentum

In this section, we start the study of the motion around a KN naked singularity. We will focus first on the “orbits” that are solutions of the following equations

$$V'(r, Q, a, L) = 0, \quad L = 0. \quad (57)$$

Note that real solutions can exist only in the case of naked singularities. This particular type of circular motion can occur in many axially symmetric spacetimes, and has been investigated in detail for neutral and charged test particles in the RN and Kerr spacetimes in [6–8]. In the RN spacetime, this particular orbit was interpreted as corresponding to a particle located at rest at $r = r_* = Q^2/M$ with respect to static observers located at infinity. The radius $r_* \equiv Q^2/M$ coincides with the value of the classical radius of an electric charge, which is usually obtained by using a completely different approach (see also [22–24]). In general, the motion defined by the conditions 57, is governed only by the gravitational component of the effective potential (and the electromagnetic interaction in the case of charged particles), with a zero centrifugal force. Therefore, if a configuration with $L = 0$ is possible, it should be the result of a balance of forces. Thus, this fact can be interpreted in terms of repulsive gravity effects. It is then important to note that these limiting conditions can exist only in the case of naked singularities, even for $a = 0$ or $Q = 0$. This means that the “repulsive component” of the effective mass in the case of a Kerr naked singularity is guaranteed by the so-called “spin-charge” of the source. The presence of both charges in the KN spacetime, in Eq. 14, makes this

effect to become more complex due to the combination of these two components. For more details about the repulsive gravitation effects in naked singularities, see also [25].

The solutions of Eq. 57 are listed in Table V and plotted in Fig. 7-Left from which it is possible to see that for

TABLE V: Description of the circular orbits for a test particle in a Kerr–Newman naked singularity with $L = 0$.

Case: $Q = 0$ (Kerr metric)		$0 < Q \leq 0.344263M$		$0.344263M < Q < \sqrt{5}M/4$	
a/M	Radius	a/M	Radius	a/M	Radius
$M < a < 3\sqrt{3}M/4$	$(\tilde{r}_2, \tilde{r}_3)$	$a_s < a < a_2$	$(\tilde{r}_1, \tilde{r}_2, \tilde{r}_3)$	$a_s < a < a_1$	\tilde{r}_1
$a = 3\sqrt{3}M/4$	\tilde{r}_2	$a = a_2$	$(\tilde{r}_1, \tilde{r}_2)$	$a = a_1$	$(\tilde{r}_1, \tilde{r}_3)$
		$a > a_2$	\tilde{r}_1	$a_1 < a < a_2$	$(\tilde{r}_1, \tilde{r}_2, \tilde{r}_3)$
				$a > a_2$	\tilde{r}_1
Case: $\sqrt{5}M/4 \leq Q \leq M$		$Q > M$			
a/M	Radius	a/M	Radius		
$a > a_s$	\tilde{r}_1	$a = 0$	Q^2/M		
		$a > 0$	\tilde{r}_1		

$Q > M$ there always exists at least one “circular orbit” radius characterized by the conditions given in Eq. 57 for $a > a_s$, and in the case of a RN naked singularity; thus, when $a = 0$ and $Q > M$, it is $r = r_* \equiv Q^2/M$. For $Q = 0$, “circular orbits” defined by Eq. 57 exist only in a closed interval $a/M \in [1, 3\sqrt{3}/4]$. A numerical analysis shows that the orbital regions in the plane (a, r) are bounded by the intrinsic spins a_1, a_2 whose exact form can be found in Appendix B.

Moreover, for $Q/M < \sqrt{5}/4$ there are several radii satisfying the conditions 57. This is a feature of the Kerr naked singularity, $Q = 0$, as well as of the KN singularity. However, in the KN case the situation is much more complex, and the possibility appears to have three radii $(\tilde{r}_1, \tilde{r}_2, \tilde{r}_3)$, but only in the range $a < a_2$. In Figs. 13 we show some specific examples of these cases. This analysis is also useful to show that eventually a minimum appears, at which these peculiar conditions are satisfied, that corresponds to the interesting case of particle at rest ($L = 0$) on a stability point.

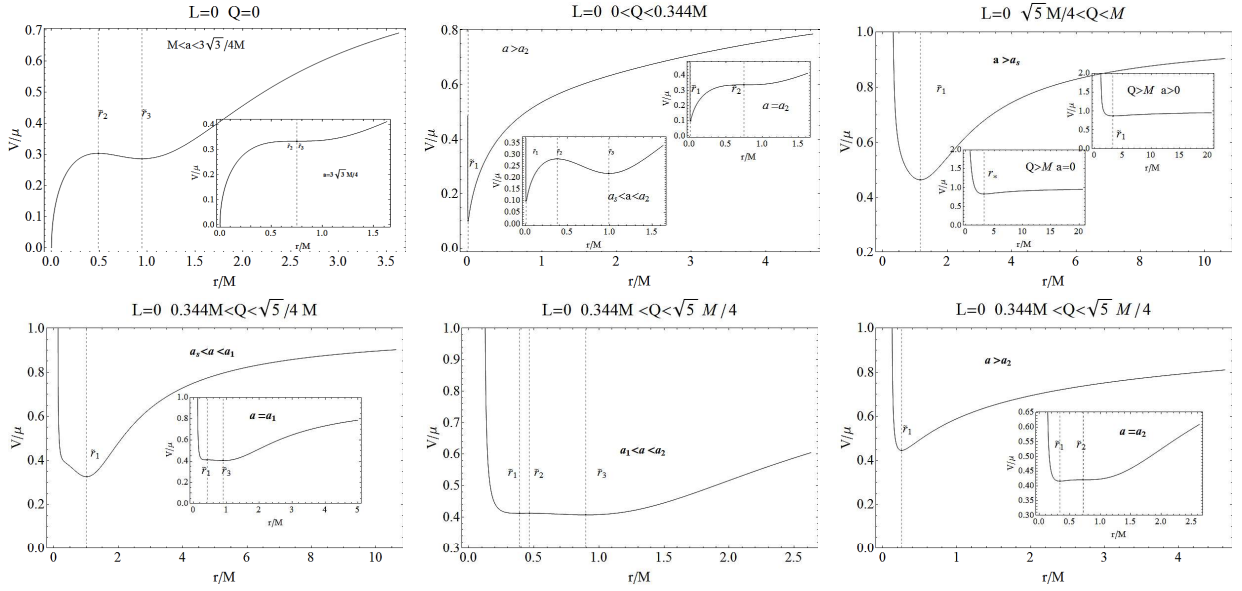


FIG. 13: The effective potential V/μ for a neutral test particle with angular momentum $L = 0$ in the field of a Kerr–Newman naked singularity with different values of Q/M and a/M . See also Table V. We also plot the radii \tilde{r}_1, \tilde{r}_2 and \tilde{r}_3 (dashed gray line).

B. Circular motion and stability problem

In this section, we focus on general circular motion with $L \neq 0$. First, it turns out to be convenient to analyze separately the case $Q > M$, in which the spacetime metric has a singularity not covered by the horizon for any value

of the spin a/M , and the case $Q \leq M$, in which the source spin must comply with the naked singularity constraint $a > a_s$. In order to simplify the discussion it is useful to analyze first the case $Q > \sqrt{3}M$; in fact from Figs. 14 and Figs. 22 – which will be discussed below – we expect for $Q \geq \sqrt{3}M$ a forbidden region only for $r < r_*$, and only three orbital regions namely (we use a classification similar to that introduced in Sec. III): region **I** characterized by $L = L_-$, region **II** with $L = (L_-, -L_+)$, and region **III** with $L = -L_+$. A fourth orbital region **IV** with $L = -L_-$ appears for $M \leq Q < \sqrt{3}M$. The characterization of circular motion for these values of charge-to-mass ratios is considerably more complex and, therefore, requires a different approach.

Thus for $Q > \sqrt{3}M$ and $0 < a < a_T$ circular orbits exist within the interval $r_* < r \leq \tilde{r}$. The explicit value of \tilde{r} depends on the ratios a/M and Q/M (see Fig. 14). It can be shown that in this interval, the orbital angular momentum is $L = -L_+$. On the other hand, for $r > \tilde{r}$ there exist circular orbits with both $L = L_-$ and $L = -L_+$. For sufficiently large values of Q/M , all these circular orbits are stable. The last stable circular orbit (r_{lSCO}) is, therefore, located at $r = r_*$, where the particle angular momentum and the energy are

$$L_*/(M\mu) = -\sqrt{\frac{a^2 M^2}{Q^2(Q^2 - M^2)}}, \quad E_*/\mu = \sqrt{\frac{Q^2 - M^2}{Q^2}}, \quad (58)$$

respectively. Note that this was exactly the case for $a = 0$, in which for $Q/M > \sqrt{5}/2$ all the orbits with $r > r_*$ were stable, while for lower values of Q/M we had a closed region of instability. The energy is always positive and independent of the value of the intrinsic angular momentum of the gravitational source; it approaches the value $E_* \rightarrow \mu$ for large values of Q (see Figs. 14).

For $\mathbf{a} > \mathbf{a}_T$ circular orbits exist at $r = r_*$ with angular momentum and energy as given in Eq.(58). For the remaining radial distances there are several possibilities. In fact, in the interval $r_* < r \leq \tilde{r}$, the orbits have $L = -L_+$, in $\tilde{r} < r < r_3$ the orbital angular momentum can be either $L = -L_+$ or $L = L_-$, in $r_3 \leq r \leq r_4$ it is $L = L_-$, and, finally, for $r > r_4$ there are circular orbits with $L = L_-$ and $L = -L_+$. The situation for $Q > \sqrt{3}M$ is summarized in Table VI.

TABLE VI: Description of the circular orbits for a test particle in a KN naked singularity with $Q > \sqrt{3}M$.

Case: $Q > \sqrt{3}M$		Angular momentum
Region		
$a > a_T$	$]Q^2/M, \tilde{r}[$	$-L_+$
	$] \tilde{r}, r_3[$	$(L_-, -L_+)$
	$] r_3, r_4[$	L_-
	$] r_4, \infty[$	$(L_-, -L_+)$
$0 < a < a_T$	$]Q^2/M, \tilde{r}[$	$-L_+$
	$] \tilde{r}, \infty[$	$(L_-, -L_+)$

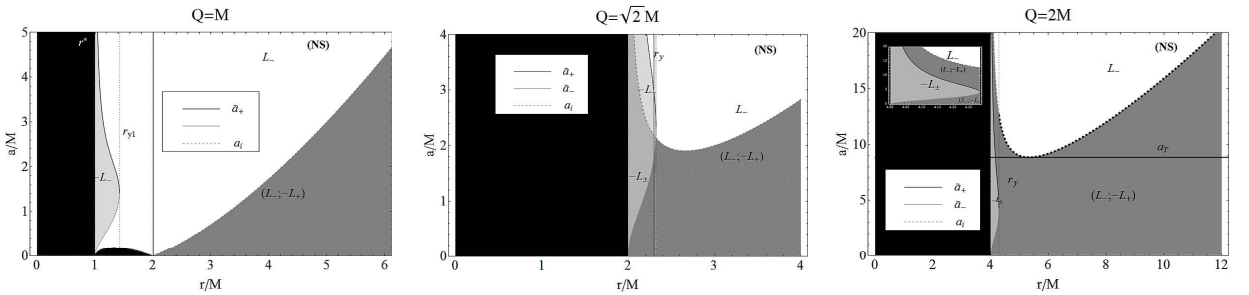


FIG. 14: Plots of the intrinsic KN angular momentum \tilde{a}_-/M (gray curve), \tilde{a}_+/M (black curve) and a_i/M (dashed gray curve) as functions of r/M , for increasing values of the charge-to-mass ratio Q/M . The angular momentum of the orbiting test particle is shown in each region. Black regions are forbidden: circular motion is not possible there. Dotted lines represent the radii r_* , r_γ^\pm and r_γ .

The case $Q < \sqrt{3}M$ requires a different analysis because there are some important details in the dynamics around naked singularities that must be emphasized. In Figs. 14, (for $Q > M$) and Figs. 15 (for $Q < \sqrt{3}/2M$), we plot the orbital radius in terms of the intrinsic angular momentum a/M for different values of Q/M . For a better presentation, we have “rotated” the figures, plotting the inverse of the function $a = a(r)$, and using the definition a_i in Eq. (41). We want to emphasize that in the plane (r, a) , these curves coincide with \tilde{r} so that the correspondence between the results in Table VI and Figs. 14 does not give rise to confusion. Thus the highlighted regions in Figs. 14 are the orbital

regions with fixed Q/M for different values of the spin. In all the cases, the region $r < r_*$ is forbidden. For $\mathbf{Q} \geq \sqrt{3}\mathbf{M}$ the situation is rather simple: As one can see in Figs. 14, and it is also shown with details in Table VI, there are three allowed orbital regions which we have denoted as follows: **I** characterized by $L = L_-$, **II** with $L = (L_-, -L_+)$, and **III** with $L = -L_+$. Using this classification, we can interpret the results in Table VI as follows: The region **III** has a finite, bounded spatial extension that reaches a maximum r_{max} at a given value of the spin a_{max} , and then decreases as the spin of the source increases. The values (r_{max}, a_{max}) depend in general on the source charge-to-mass ratio Q/M . The size of this region increases with increasing Q/M . The regions **I** and **II**, instead, have an infinite extension.

The situation for $\mathbf{M} < \mathbf{Q} < \sqrt{3}\mathbf{M}$ is much more complex and in addition to the three orbital regions, which characterize the motion in $Q \geq \sqrt{3}M$, there is now a fourth orbital region **IV** with $L = -L_-$. The size of the orbital region **IV** increases as Q/M decreases. Instead, the region **III** decreases with decreasing Q/M until it disappears in the limit $Q = M$ (see Fig. 14). The orbital region **IV** increases until it reaches a maximum and then decreases. The figure highlights the presence of a further type of naked singularity for $Q^2 < (9/8)M^2$; in fact, for $Q^2 = (9/8)M^2$, an additional banned orbital zone appears for $a < a_i$ and $r < r_\gamma^+$. This zone increases as Q/M increases, and for fixed values of a/M and Q/M it is localized in a finite spatial region. Notice that at $r > r_\gamma^+$ there are orbits for spin $a < a_i$ with $(L_-, -L_+)$, that is, there exists a region of type **II**. In Table VII, we include the different cases.

TABLE VII: Description of the circular orbits for a test particle in a Kerr–Newman spacetime. At $r = r_y$ it is $\tilde{a}_+ = \tilde{a}_-$. In the naked singularity case for $Q < M$, it is always $a > a_s$. And $a_i < a_s$ in $r \in]r_d^-, r_d^+[$, whereas $a_i = a_s$ for r_d^\pm and $r = M$. See also Appendix A and Figs. 22.

$0 < Q < M$		NS-III: $M < Q < \sqrt{9/8}M$		NS-II: $\sqrt{9/8}M < Q < \sqrt{3}M$		NS-I: $Q > \sqrt{3}M$	
$r_* < r < r_y$		$r_* < r < r_\rho$		$r_* < r < r_y$			
$a_i < a < \tilde{a}_-$	L_-	$0 < a < \tilde{a}_-$	$(L_-, -L_+)$	$0 < a < \tilde{a}_-$	$(L_-, -L_+)$	$0 < a < \tilde{a}_-$	$(L_-, -L_+)$
$\tilde{a}_- < a < \tilde{a}_+$	$-L_-$	$\tilde{a}_- < a < a_i$	$-L_\pm$	$a_i < a < \tilde{a}_-$	$-L_\pm$	$\tilde{a}_- < a < \tilde{a}_+$	$-L_\pm$
$a > \tilde{a}_+$	L_-	$a_i < a < \tilde{a}_+$	$-L_-$	$\tilde{a}_+ < a < a_i$	$-L_-$	$\tilde{a}_+ < a < a_i$	$(L_-, -L_+)$
		$a > \tilde{a}_+$	L_-	$a > \tilde{a}_+$	L_-	$a > a_i$	L_-
$r_y < r < r_\gamma^+$		$r_\rho < r < r_\gamma^-$		$r > r_y$			
$a > a_i$	L_-	$0 < a < a_i$	$(L_-, -L_+)$	$0 < a < a_i$	$(L_-, -L_+)$	$0 < a < a_i$	$(L_-, -L_+)$
		$a_i < a < \tilde{a}_-$	L_-	$a > a_i$	L_-	$a > a_i$	L_-
		$\tilde{a}_- < a < \tilde{a}_+$	$-L_-$				
		$a > \tilde{a}_+$	L_-				
$r > r_\gamma^+$		$r_\gamma^- < r < r_y$					
$0 < a < a_i$	$(L_-, -L_+)$	$a_i < a < \tilde{a}_-$	L_-				
$a > a_i$	L_-	$\tilde{a}_- < a < \tilde{a}_+$	$-L_-$				
		$a > \tilde{a}_+$	L_-				
		$r > r_\gamma^+$					
		$0 < a < a_i$		$(L_-, -L_+)$			
		$a > a_i$		L_-			

Finally for $\mathbf{Q} < \mathbf{M}$, and $a > a_s$ (condition of existence of a naked singularity with $Q < M$, Eq. (21), the analysis is schematically summarized in Figs. 15. Some examples are discussed in Appendix. B. We note that the region **IV**,

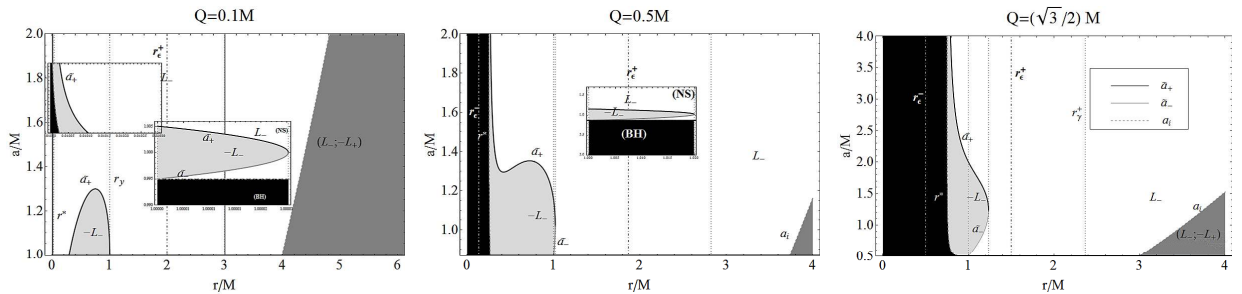


FIG. 15: Plots of the intrinsic KN angular momentum \tilde{a}_-/M (gray curve), \tilde{a}_+/M (black curve) and a_i/M (dashed gray curve) as functions of r/M , for increasing values of the charge-to-mass ratio $Q/M = 0.1, 0.5, 0.866025$. The region $a > a_s$ is explored: a naked singularity occurs for $Q < M$ and $a > a_s$. The angular momentum of the orbiting test particle is shown in each region. Black region $r < r_*$ is forbidden; no circular motion is possible there. The dotted-dashed line is the outer ergosphere r_e^+ .

with $L = -L_-$, has a very complex structure and, in contrast to the case. $M \leq Q < \sqrt{3}M$, it not only possesses a maximum at r_{max} , but also a minimum r_{min} that appears as the charge decreases. This situation is illustrated for $Q = 1/2M$ in the central plot of Fig. 15. We see that, for a suitable range of values of the source angular momentum, as the radial distance increases there appear two disconnected regions of type **IV**. This situation becomes extreme with decreasing values of Q/M ; for instance, for $Q = 1/10M$ the two regions are completely separated. The outer region, farthest from the singularity, has a finite extension and the inner region, closer to the singularity, has an infinite extension.

The radius at which the region **II**, with $(L_-, -L_+)$, starts, increases as the source charge-to-mass ratio Q/M decreases. This can be interpreted as a consequence of the fact that the effects due to the spin become increasingly predominant as the charge decreases, affecting the properties of the counter-rotating orbits with $L = -L_+$. As a result, circular motion is no more allowed at very close to the central source where the effects of the gravitational stress due to the singularity are expected to be very strong. This effect is corroborated by the fact that a similar behavior is found when the charge remains fixed and the spin of the source is increased.

It is important to notice that once the two parameters $(a/M, Q/M)$ are fixed within in a suitable interval, the regions where circular orbits are allowed become disconnected. In particular, for $Q < M$ and orbits sufficiently close to the singularity, the regions affected by this phenomenon are of the types **IV** and **I**.

As a result of this analysis, we can identify four types of naked singularities according to the charge-to-mass ratio:

NS-I : For $Q/M \geq \sqrt{3}$ with orbital regions of the type **I**, **II** and **III**

NS-II : For $3/2\sqrt{2} \leq Q/M < \sqrt{3}$ with orbital regions of the type **I**, **II**, **III**, **IV** and one forbidden region

NS-III : For $1 < Q/M < 3/(2\sqrt{2})$ with orbital regions of the type **I**, **II**, **III**, **IV** and two forbidden regions

NS-IV : For $Q/M < 1$ with orbital regions of the type **I**, **II** and **IV**

Notice that in naked singularities of the type **NS-IV**, it is necessary to consider the position of the ergosphere region $[r_\epsilon^-, r_\epsilon^+]$, because, as shown in Figs. 15, in this case $r < r_\epsilon^+$.

The results of studying the problem of stability are represented in Figs. 16. The open curves shown in Figs. 12 for

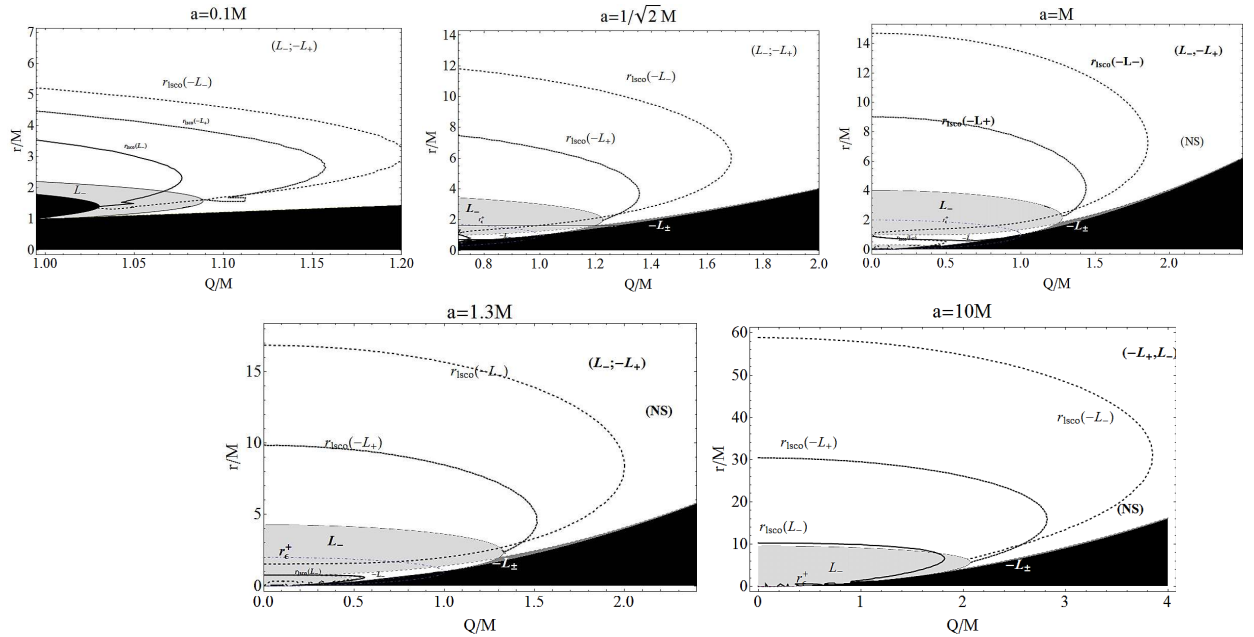


FIG. 16: The charge-to-mass ratio Q_T^\pm/M , Q_*/M and Q_{c2} as functions of r/M , for increasing values of the source spin. The angular momentum of the orbiting test particle is denoted in each region. Black regions are forbidden. The radius of the last stable circular motion r_{lSCO} is plotted: $r_{lSCO}(L_-)$ (thick black curve), $r_{lSCO}(-L_-)$ (thick black dashed curve) and $r_{lSCO}(-L_+)$ (thick black dotted curve). In the region $r < r_{lSCO}$ ($r > r_{lSCO}$), circular orbits are unstable (stable). A naked singularity occurs for $a > M$ and $Q > Q_s$; then, $Q_s = 0.994987M$ for $a = 0.1M$, $Q_s = 0.707107M$ for $a = 1/\sqrt{2}M$ and $Q_s = 0$ for $a = M$. The dotted-dashed curve is the ergosphere boundary r_ϵ .

black holes, find a smooth continuation here in the naked singularity case, as illustrated in Figs.16. As a result, for

fixed values of Q/M , a finite region of instability appears that splits the plane into two regions of stability. The plots show a disconnected structure that resembles the structures found previously in the case of RN [6] and Kerr [7] naked singularities.

Several features appear in the case of naked singularities. Firstly, there is a new region of exclusively counter-rotating orbits (type **III**) that is practically always stable. Also, in general, the radii of the orbits r_{lsc} intersect now at a point, thereby creating a complex structure which depends on the source spin and charge. The region **I**, which is closer to the singularity (say at $r \lesssim 5M$), presents the most complex structure so that by varying a/M , we can have regions completely filled with either stable or unstable orbits or also partially filled with stable and unstable orbits. In this regard, for small enough spin (say approximately $a < 10M$), the region **I** splits into two disconnected regions that become larger as a/M decrease, until they become entirely separated by a type **IV** region ($L = -L_-$), as illustrated in Figs. 23. This region appears to be always unstable and is bounded by the curve $r_{lsc}(L_-)$. Then, the region of instability, which increases with increasing a/M , will eventually cover at $a = 10M$ the single type **I** region, which therefore results in an almost complete island of instability. For sufficiently large values of a/M , the radius $r_{lsc}(L_-) > r_e^+$.

In conclusion, the existence, extent and stability properties of the region **I** is mainly determined by the spin of the source.

V. BLACK HOLES VS NAKED SINGULARITIES

This section summarizes the main results concerning the circular motion and stability properties obtained for the black hole case in Sec. III and for the naked singularity case in Sec. IV. We show a benchmarking and discuss the key differences between these two cases. We start by considering the extension of the stability analysis performed in Sec. III and illustrated in Figs. 12 to include the naked singularity region. The left plot show the case $Q = 0$ (Kerr

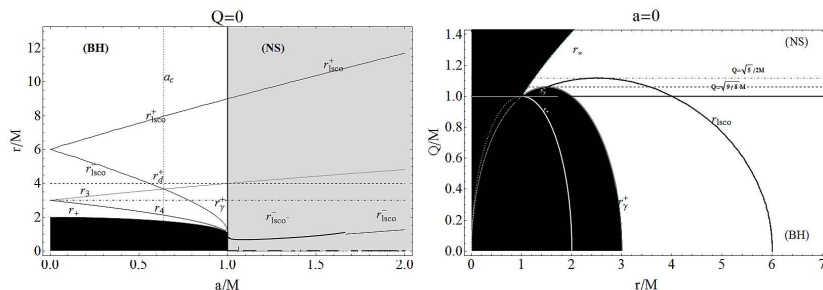


FIG. 17: Left: The radii $r_{lsc}^+ \equiv r_{lsc}(-L_+)$, $r_{lsc}^- \equiv r_{lsc}(L_-)$, and $r_{lsc}^- \equiv r_{lsc}(-L_-)$ of the last stable circular orbit in the Kerr spacetime as functions of the source angular momentum a . The horizon r_+ and the radii r_γ^+ (dotted line), r_d^+ (dashed line), r_3 (black curve), and r_4 (gray curve) are also plotted. The black region ($r < r_+$) is forbidden. The value a_c , at the crossing point between r_3 and r_{lsc}^- , is represented by a dashed line. The gray banned regions correspond to the naked singularity case (NS), the white ones to the black hole case (BH). Right: The last stable circular orbit radius r_{lsc} in the Reissner-Nordström spacetime for a black hole $Q \leq M$ and a naked singularity $Q > M$ with different charge-to-mass ratios Q/M .

spacetime) discussed in Sec. III and extensively studied in [7]. For all values of a/M , the last stable circular orbit $r_{lsc}(-L_+)$ exists, that is, for a naked singularity it is the continuous extension of the radius for the black hole case. On the other hand, the radius r_{lsc}^- , the last stable circular orbit in the black hole case with momentum $L = L_-$, does not extend to the values $a > M$. Then, in accordance with [7], two additional radii determining the stability of circular motion appear: the radius $r_{lsc}(-L_-)$ for $1 < a/M < 3\sqrt{3}/4$ and $r_{lsc}(L_-)$ for $a/M > 3\sqrt{3}/4$. The introduction of a source charge changes qualitatively the stability pattern. Firstly, the behavior of the two radii with domain only in the naked singularity region drastically depends on the value of Q/M . A similar behavior characterized the case $a = 0$. Indeed, as shown in the naked singularity case in Sec. III for sufficiently small charge source $1 < Q/M < \sqrt{9/8}$, there appears only one r_{lsc} , while in the range $1 < Q/M < \sqrt{5/2}$ the curve r_{lsc} changes direction so that for $Q/M > \sqrt{5/2}$ all allowed orbits are stable.

The stability analysis of the naked singularity case must be carried out in detail for orbital regions near the singularity. We will do this by using the analysis performed in Sec. IV for a naked singularity, by extending the results of Figs. 16 to the black hole case, and by matching Figs. 12-Right and Figs. 16. We will also use all the quantities introduced in Sec. II A. Thus, the analysis will be carried out in parallel in two alternative ways: (1) We reinterpret the analysis in Figs. 17 by studying the function $r = r(a)$: by fixing a particular value of the charge-to-mass ratio, we vary the source spin in order to cover both the black hole and the naked singularity regions. However, it

turns out to be convenient to use the inverse function $a = a(r)$ Figs. 17. The obtained regions are the same as in Figs. 17, but with a suitable enlargement of some regions close to the singularity. This is the generalization of the work performed in [7] to include a charge-to-mass ratio. This analysis turns out to be very useful to understand the main difference between the allowed regions for the circular motion around the two sources. **(2)** In the second analysis, we fix the source spin a/M and vary the charge Q/M to study the orbits $r = r(Q)$. This is a generalization of the case $a \neq 0$ of the left plot of Fig. 17 for the RN spacetime. This allows us to determine how the rotation of the source affects the results of the plot. This is the generalization of the work performed in [6] to take into account the spin-to-mass ratio. It turns out also in this case to be convenient to use the inverse function $Q = Q(r)$ in order to explore the details of the orbital regions. This comparative analysis is very important to study in detail the stability properties of the circular motion around black holes and naked singularities.

A. Comparative analysis of the circular motion

We now summarize the results of comparing the properties of circular motion in the entire KN spacetime. It is convenient to confront our results with those obtained for the limiting cases $a = 0$ and $Q = 0$, which were presented in [6–8], and are here schematically represented in Figs. 17. It was found that black holes and naked singularities are characterized by connected and disconnected regions of stability, respectively. The analysis of the generalization that includes the spin and charge of the source simultaneously is shown in Figs. 18–21 for a varying charge-to-mass ratio for selected and increasing values of the spin a/M . Figures 22 show the behavior of the circular orbits in terms of the spin a/M , for selected and increasing values of the charge Q/M .

We first consider the analysis of Figs. 18–20. The regions of existence of circular orbits with their orbital moments are marked in white and gray, while the black regions are those in which the motion is not possible. In Fig. 18, we consider the particular case $a = 0.1M$ and explore the circular orbit properties for both the black hole and naked singularity fields. Notice that from a physical point of view, in the case of black holes, we are interested in the motion outside the outer horizon only, $r > r_+$, which in the plots corresponds to the range $[r_+, +\infty[\cup[0, a_s] \cup [0, Q_s]$. Nevertheless, to understand better the behavior of the relevant radii and for the sake of completeness, we include some plots of spatial regions located very closed to the origin.

In Figs. 19 and 20, we consider the cases $a = 0.8M$ and $a = M$, respectively. We see that the location of the regions where circular motion is allowed depends drastically on the value of the ratios a/M and Q/M .

We summarize the analysis in Fig. 21, where we show the behavior of the orbital radius for increasing values of the source angular momentum. As pointed out in Sec. IV, it is possible to distinguish four different regions where circular motion is allowed with different orbital angular momenta: The region **I** with $L = L_-$, **II** with $L \in (L_-, -L_+)$, **III** associated to $L = -L_\pm$ and, finally, the region **IV** with $L = -L_-$. The region $r < r_*$ (or equivalently $Q > Q_*$) is forbidden for both black holes and naked singularities. A second forbidden region appears for configurations with $a < M$ and $Q < Q_T^-$. This region becomes smaller as a/M approaches the value $a = M$, where it disappears. We note the peculiar value $a/M = 1/\sqrt{2}$ which determines the interval $1/\sqrt{2} < a/M < 1$, where the two forbidden regions are completely disconnected and separated on the left by a region with $L = -L_-$ and on the right by a region with $L = L_-$. In other words, for $a \lesssim 1.299M$ there exist two closed regions with $L = L_-$ which are disconnected, becoming connected in a particular region for larger values of a/M . The region with $L = -L_\pm$ exist within the interval $Q_c < Q < Q_*$. The open range with $L = -L_+$ and $L = L_-$ begins in the region $r > r_x$. Furthermore, the region with $L = -L_-$ becomes smaller as a/M increases to become practically nil as the area of the region $L = -L_\pm$. The region with orbits L_- becomes increasingly wider as the intrinsic angular momentum and the charge of the source increase. We conclude that the structure of the orbital regions around a KN source is very complex in the intervals $a < M$ and $r < r_{M_2}$.

As seen in Sec. III, an alternative way to study the neutral test particle circular motion in a KN spacetime is to explore the orbital regions, for different values of the ratio a/M , as functions of the radial coordinate. This is particularly suitable in order to compare the results with those of the Kerr spacetime depicted in the left plot of Fig. 17. In Fig. 22, we show the behavior of the circular orbits for different values of the charge-to-mass ratio of the source. In this case, fixing the source charge and varying its intrinsic angular momentum, we plot the regions where circular motion occurs and point out the value of the orbital angular momentum associated with each region. The boundaries of the regions are defined by the intrinsic spin \tilde{a}_\pm and a_i . For $Q < M$ there are essentially three types of orbital regions characterized respectively by $L = -L_-$, $L = L_-$, and $L = (L_-, -L_+)$. We can see that there are two forbidden regions, the first determined by the conditions $r < r_*$ and $a < a_i$ for $Q^2/M^2 < 9/8$, and the second one by $r < r_*$ for $Q^2/M^2 \geq 9/8$. The region within the interval $(L_-, -L_+)$ increases as Q/M increases, while the regions with $L = -L_-$ and $L = L_-$ decrease as Q/M increases and, finally, they coincide at $r = r_*$. Interestingly, the region with $L = -L_-$ disappears for $Q^2/M^2 > 3$.

One can see that the orbital region ($L = L_-$) diminishes as the parameters Q/M and a/M decrease, and that

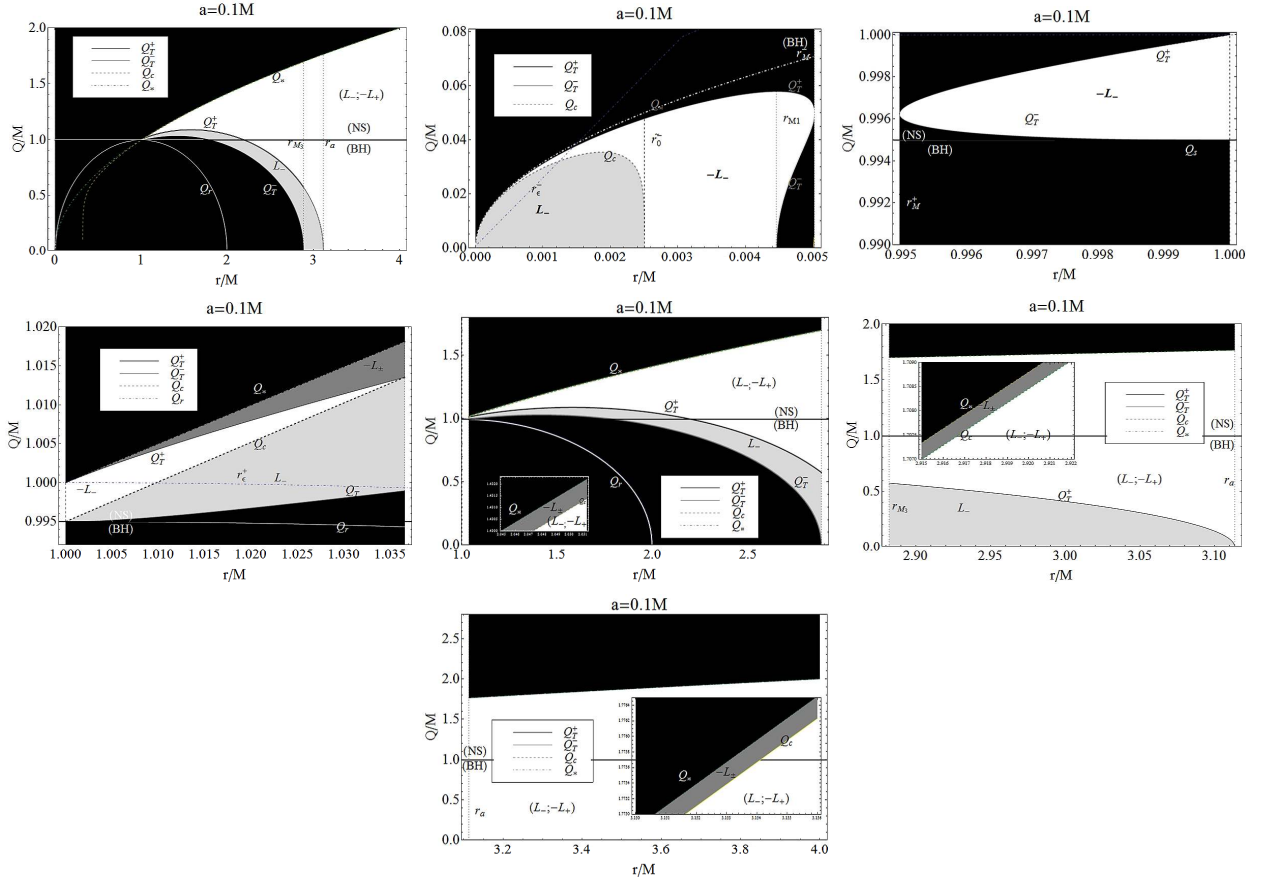


FIG. 18: The case: $a = 0.1M$. Properties of circular orbits in a KN spacetime, including black holes and naked singularities. The charge-to-mass ratio Q_T^\pm/M , Q_*/M and Q_{c2} are plotted as functions of r/M . The value of the angular momentum of the orbiting test particle is shown in each region. Black regions are forbidden; no circular motion is possible there. Dotted lines represent the radii \tilde{r}_0 , r_{M2} , and r_* . Upper-left shows the range $r/M \in [0, 4]$. The remaining plots magnify the intervals where non-trivial behaviors are observed. The solid (dashed) white curve is the outer (inner) horizon r_+ (r_-). We denoted with \tilde{r}_0^- the lowest value of $\tilde{r}(Q = 0)$. The horizontal thick black line represents $Q = Q_s$. A naked singularity occurs for $a > M$ and $Q > Q_s$, i.e., $Q_s = 0.994987M$ in this case. The black hole (BH) and naked singularity (NS) regions are denoted explicitly. The dotted-dashed curve represents the ergosphere boundaries r_\pm^\pm .

it extends from a rather small distance from the central source (light gray region). For Q/M small enough, say $Q \ll M/2$, this region disappears and, as the charge increases, it moves towards areas with higher spin and smaller radii. For $Q > M$ a new orbital region appears, characterized by two different types of counter-rotating orbits with $L = -L_\pm$; this region becomes increasingly larger as the ratio $Q > M$ increases. Finally, we note that the regions with $L = -L_\pm$ and $L = -L_-$ are bounded and extend up to a maximum radius and a maximum angular momentum of the source.

The curve $a = a_i$ divides the plot into two regions, the left black one, in which no circular motion is allowed, and the right one, in which orbital motion occurs for $a > a_i$ with $L = L_-$ and for $a < a_i$ with $L = (L_-, -L_+)$. As the source spin increases, the left forbidden region first grows to a maximum value of the orbital radius and then begins to decrease. On the other hand, the region with $L = (L_-, -L_+)$ (right gray region) covers larger orbital radii as the spin increases, and moves towards the central source as the charge-to-mass ratio decreases.

B. Discussion of the stability problem

In this last section, we will study the influence of the intrinsic angular momentum and charge of the source on the stability properties of test particles, moving along circular orbits around the central source. In Sec. III B and Sec. IV B, we studied the case of a black hole and a naked singularity, respectively. In Fig. 23, we show a review of the results when both sources are analyzed simultaneously. First, we note the presence of last stable circular orbit radii r_{lsc0} for all possible orbits with angular momentum $-L_+$, $-L_-$ and L_- . The location of r_{lsc0} depends on the value

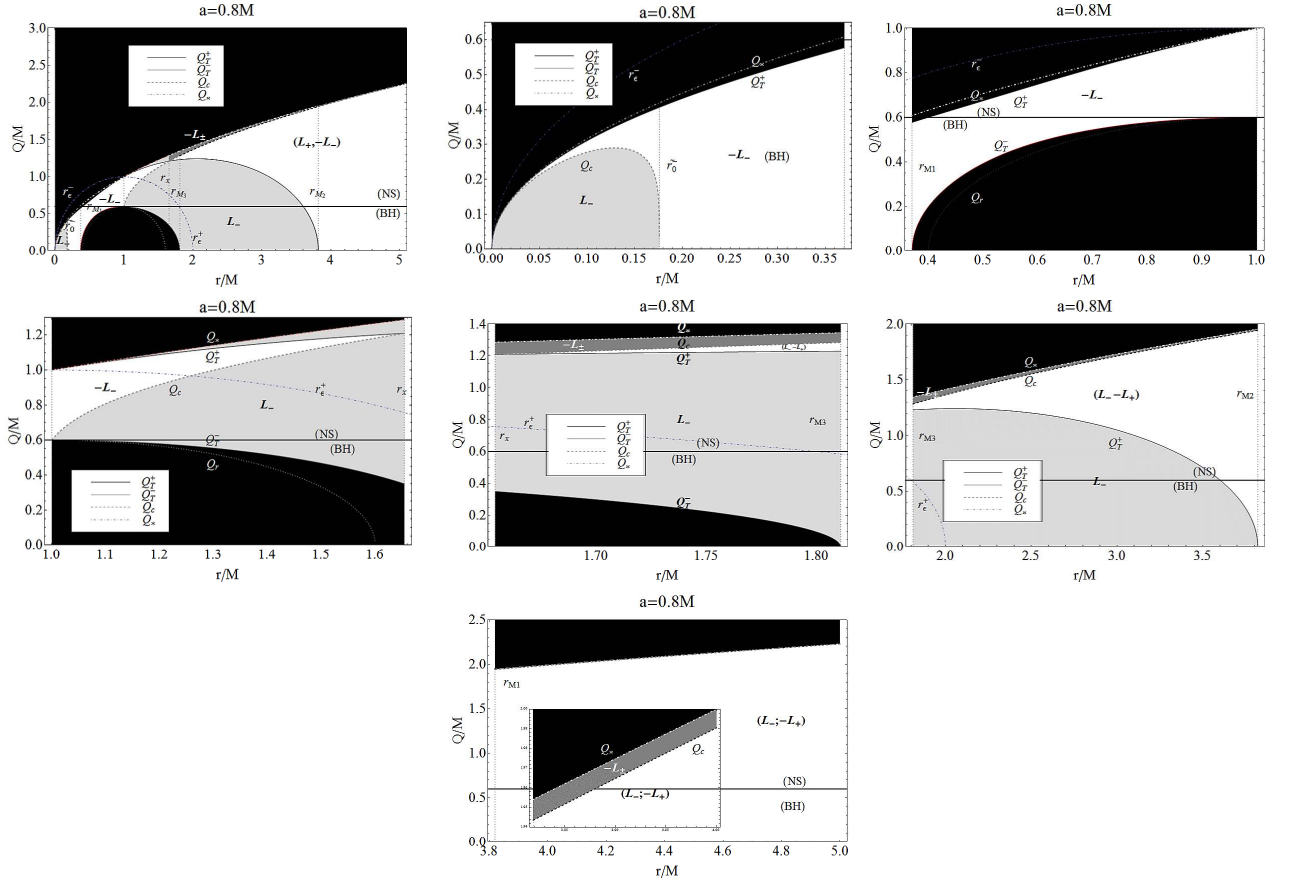


FIG. 19: The case: $a = 0.8M$. Properties of circular orbits in a KN spacetime, including black holes and naked singularities. The charge-to-mass ratio Q_{T}^{\pm}/M , Q_{*}/M and Q_{c2} are plotted as functions of r/M . The angular momentum of the orbiting test particle is shown in each region. Black regions are forbidden; no circular motion is possible there. Dotted lines represent the radii \tilde{r}_0 , r_{M2} , r_{M3} , r_{*} , r_x . Upper-left shows the range $a/M \in [0, 5]$. The remaining plots magnify the intervals where non-trivial behaviors are observed. The solid (dashed) white curve is the outer (inner) horizon r_+ (r_-). We denoted with \tilde{r}_0^- the lowest value of $\tilde{r}(Q = 0)$. The horizontal thick black line represents $Q = Q_s$. A naked singularity occurs for $a > M$ and $Q > Q_s$, i.e., $Q_s = 0.6M$ in this case. The black hole (BH) and naked singularity (NS) regions are denoted explicitly. The dotted-dashed curve represents the ergosphere boundaries r_{ϵ}^{\pm} .

of the intrinsic angular momentum. The larger is the rotation, the further from the origin is r_{lsc0} . This is physically reasonable since the rotation is known to generate its own gravitational field in general relativity. On the other hand, for a fixed value of a/M , as the charge-to-mass ratio increases, the value of r_{lsc0} first increases until it reaches a maximum value and then it decreases. We have, in general, that $r_{lsc0}(L_-) > r_{lsc0}(-L_+) > r_{lsc0}(-L_-)$, but this situation becomes significantly more complex with increasing spin and decreasing source charge.

To formulate the main results in a plausible manner, let us imagine an idealized accretion disk made of test particles which are moving along circular orbits on the equatorial plane of a KN spacetime. It then follows that the structure of the accretion disk will be determined by the locations of the radii of the last stable circular orbits. Consider, for instance, in Fig.23 the case $a = 0.9M$. The radius $r_{lsc0}(L_-)$ determines the minimum radius of the idealized accretion disk which in the case of a black hole could be extended, in principle, to infinity, because the stability zone has no upper bound. The situation is different in the case of a naked singularity. The disconnected structure of the stability regions is especially clear for $a > M$. However, for $a = 0.9M$, for example, the radius $r_{lsc0}(-L_+)$ clearly goes into the NS zone creating a stable (left) orbital region with $L = -L_+$, an unstable region limited by $r_{lsc0}(-L_+)$, and a stable region (right) for $r > r_{lsc0}(-L_+)$. This situation does not occur in the black hole case. Notice a second unstable region of type L_- separated by a stable zone (right) from a $-L_-$ region.

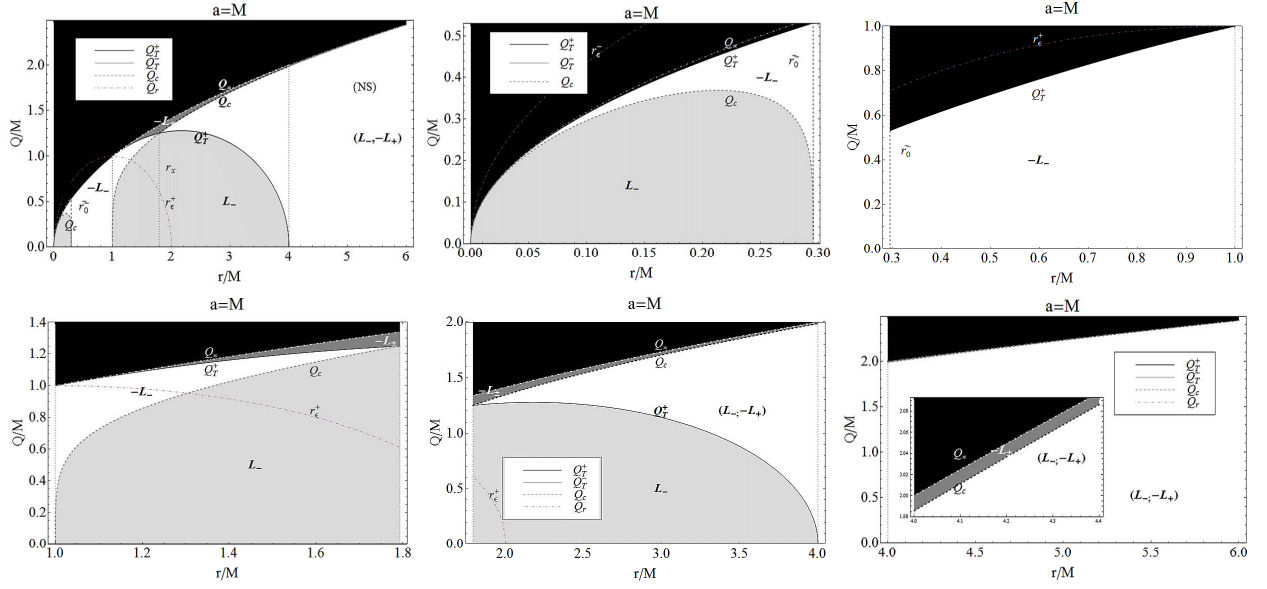


FIG. 20: The case: $a = M$. Properties of circular orbits in a KN spacetime, including black holes and naked singularities. The charge-to-mass ratio Q_{\pm}^{\pm}/M , Q_*/M and Q_{c2} are plotted as functions of r/M . The dotted-dashed curve represents the ergosphere boundaries r_{ϵ}^{\pm} . The angular momentum of the orbiting test particle is shown in each region. Black regions are forbidden; no circular motion is possible there. Dotted lines represent the radii \tilde{r}_0 , r_* , r_x . Upper-left shows the range $a/M \in [0, 6]$. The remaining plots magnify the intervals where non-trivial behaviors are observed. The solid (dashed) white curve is the outer (inner) horizon r_+ (r_-). We denoted with \tilde{r}_0^- the lowest value of $\tilde{r}(Q = 0)$. A naked singularity occurs for $a > M$ and $Q > Q_s$, i.e., $Q_s = M$ in this case.

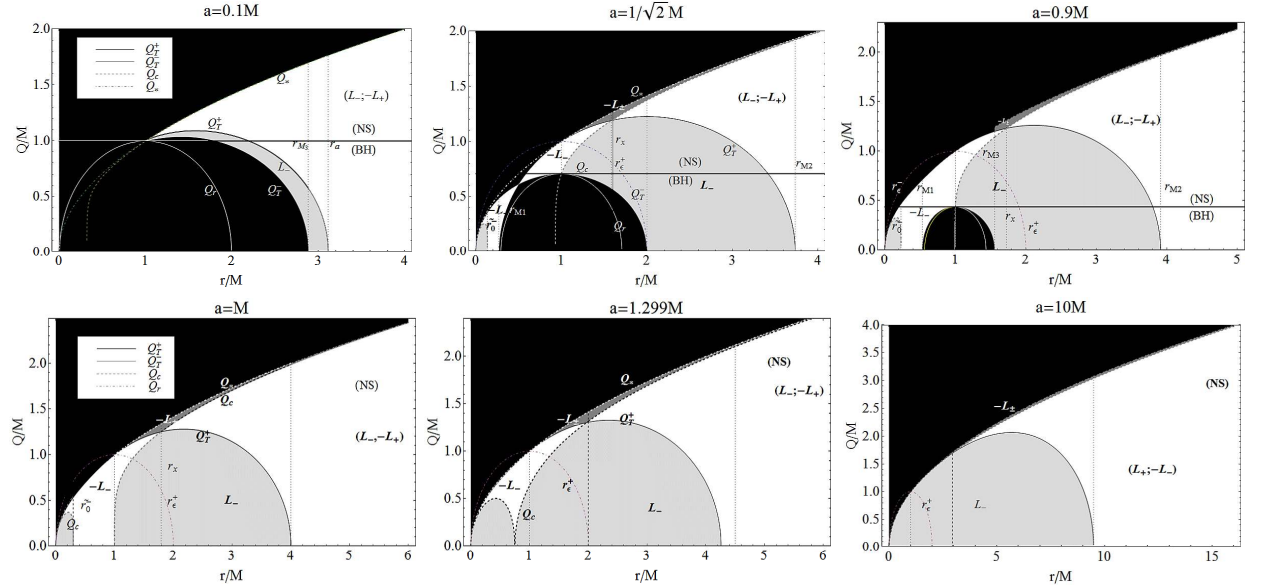


FIG. 21: The charge-to-mass ratio as a function of the radial coordinate for increasing values of the source angular momentum. The ratios Q_{\pm}^{\pm}/M , Q_*/M and Q_{c2} are also plotted. The angular momentum of the orbiting test particle is shown in each region. Black regions are forbidden; no circular motion is possible there. Dotted lines represent the radii \tilde{r}_0 , r_* , and r_x . We denoted with \tilde{r}_0^- the lowest value of $\tilde{r}(Q = 0)$. The horizontal thick black line represents $Q = Q_s$. A naked singularity occurs for $a > M$ and $Q > Q_s$, i.e., $Q_s = 0.994987M$ for $a = 0.1M$, $Q_s = 0.707107M$ for $a = 1/\sqrt{2}M$, $Q_s = 0.43589M$ for $a = 0.9M$ and $Q_s = 0$ for $a = M$. The black hole (BH) and naked singularity (NS) regions are denoted explicitly. The dotted-dashed curve represents the ergosphere boundaries r_{ϵ}^{\pm} .

VI. CONCLUSIONS

In this work, we performed a detailed analysis of the behavior of test particles moving along circular orbits on the equatorial plane of the KN spacetime. We use the method based on the investigation of the effective potential from

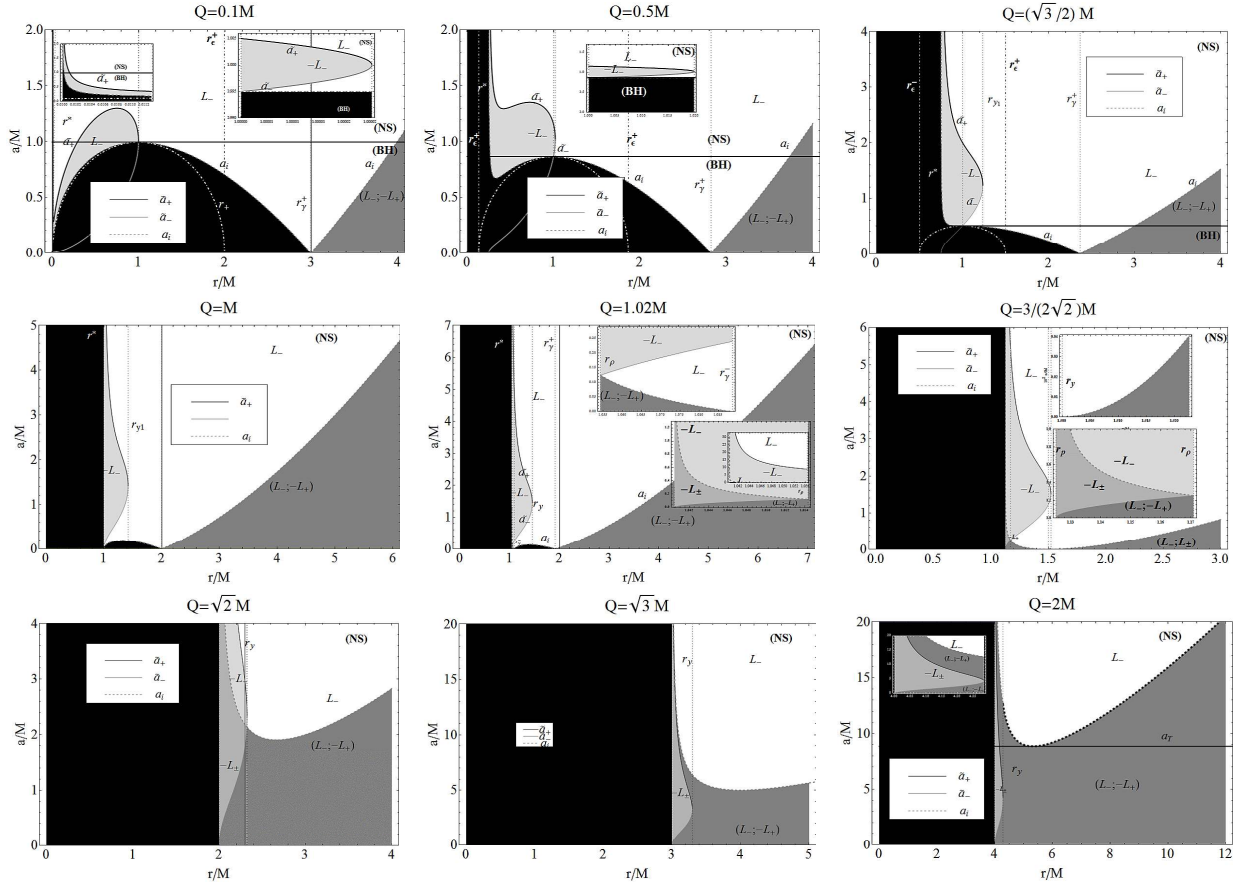


FIG. 22: The intrinsic KN angular momentum \tilde{a}_-/M (gray curve), \tilde{a}_+/M (black curve) and a_i/M (dashed gray curve) as functions of r/M , for increasing values of the charge-to-mass ratio Q/M . The angular momentum of the orbiting test particle is shown in each region. Black regions are forbidden; no circular motion is possible there. Dotted lines represent the radii r_* , r_γ^\pm and r_z . The dotted-dashed white curve is the outer horizon r_+ . The dotted-dashed black curve represents the ergosphere boundaries r_ϵ^\pm . The thick black horizontal line is $a = a_s$; a naked singularity occurs for $Q < M$ and $a > a_s$. The black hole (**BH**) and the naked singularity (**NS**) regions are explicitly denoted. In this case, $a_s = 0.994987M$ for $Q = 0.1M$, $a_s = 0.866025M$ for $Q = 0.5M$, and $a_s = 0.5$ for $Q = \sqrt{3}/2M$.

which one can derive the location and the stability properties of the circular orbits. We also analyzed the energy and angular momentum of all possible orbits, and used this information to identify different orbital regions which allow us to find out the differences between black holes and naked singularities.

We have identified four orbital regions, namely: region **I** characterized by $L = L_-$, region **II** with $L = (L_-, -L_+)$, region **III** with $L = -L_\pm$, and a fourth orbital region **IV** with $L = -L_-$. The region **I** contains only co-rotating particles whereas regions **III** and **IV** are for counter-rotating particles. It is interesting that region **II** contains both co-rotating and counter-rotating particles with different orbital angular momentum.

We found that naked singularities can be divided into four classes that depend on the value of the charge-to-mass ratio: **NS-I** for $(Q/M \geq \sqrt{3})$ with orbital regions of the type **I-II-III**, **NS-II** for $(3/(2\sqrt{2}) \leq Q/M < \sqrt{3})$ with orbital regions of the type **I-II-III-IV** and one forbidden region, **NS-III** for $(1 < Q/M < 3/(2\sqrt{2}))$ with orbital regions of the type **I-II-III-IV** and two forbidden regions and **NS-IV** for $(Q/M < 1)$ with orbital regions of the type **I-II-IV**. Figure 24 illustrates this classification also for the case of black holes.

We found that from the point of view of the circular motion, there exists always a forbidden area ($r < r_*$) which is completely inaccessible for test particles. In the case of black holes, the radius r_* is situated inside the outer horizon. In the case of naked singularities, it can be considered as a surface that ‘‘covers’’ the singularity itself and prevents it from being studied with orbiting test particles. The value of the radius $r_* = Q^2/M$ does not depend on the source angular momentum so that it is a property of the gravitational field generated only by the electric charge only. It is interesting that the expression for r_* coincides with the classical radius of an electric charge Q with mass M which is obtained by applying a completely different approach. In the limiting case of a RN naked singularity, this radius has a very particular significance because it corresponds to particles with vanishing angular momentum ($L = 0$) [6].

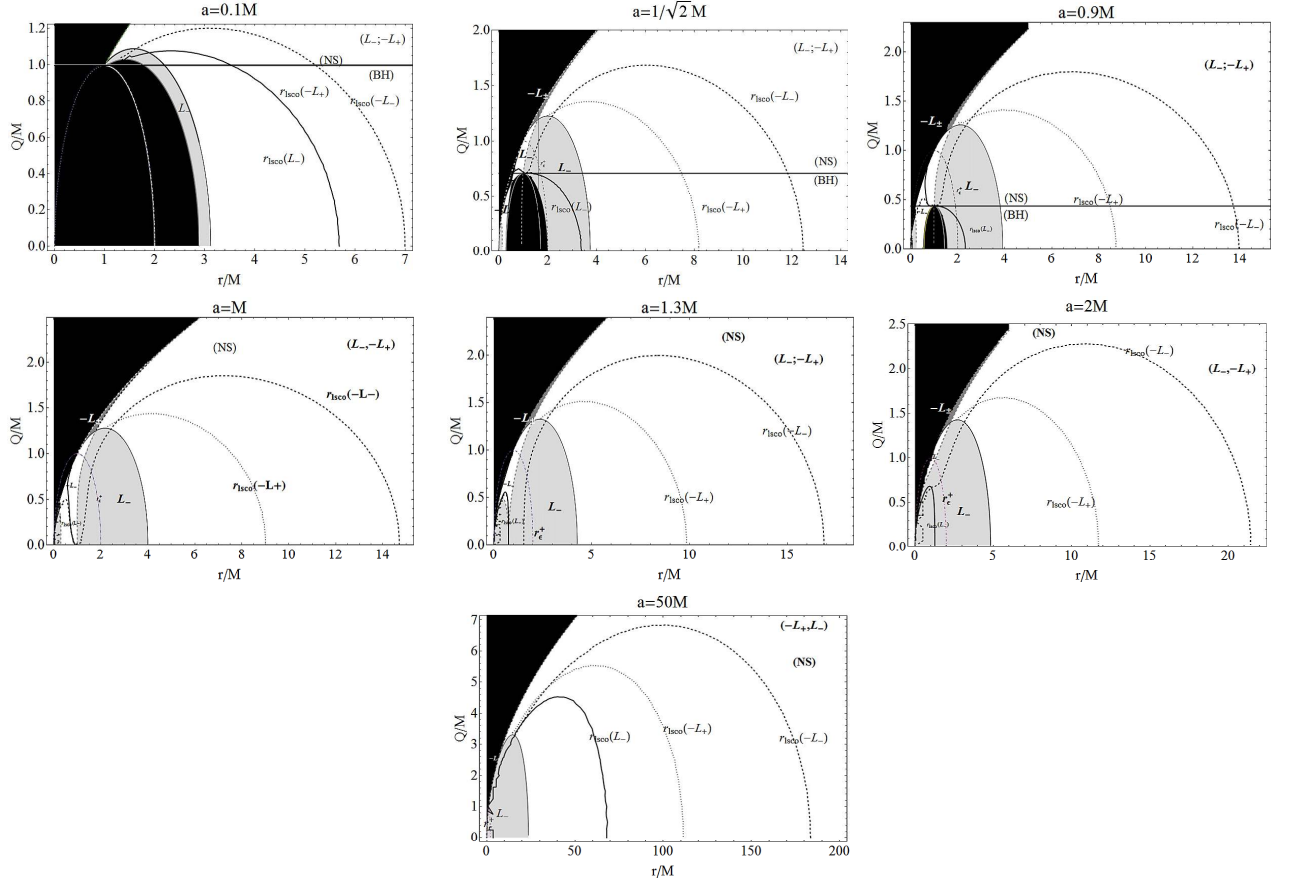


FIG. 23: The charge-to-mass ratios Q_{\mp}^{\pm}/M , Q_{*}/M and Q_{c2} as functions of r/M , for increasing values of the source spin. The angular momentum of the orbiting test particles is shown in each region. Black regions are forbidden. The radius of the last stable circular motion r_{lSCO} is plotted: $r_{lSCO}(L-)$ (thick black curve), $r_{lSCO}(-L-)$ (thick black dashed curve) and $r_{lSCO}(-L+)$ (thick black dotted curve). In the region $r < r_{lSCO}$ ($r > r_{lSCO}$), circular orbits are unstable (stable). The horizontal thick black line represents $Q = Q_s$. A naked singularity occurs for $a > M$ and $Q > Q_s$, i.e., $Q_s = 0.994987M$ for $a = 0.1M$, $Q_s = 0.707107M$ for $a = 1/\sqrt{2}M$, $Q_s = 0.43589M$ for $a = 0.9M$ and $Q_s = 0$ for $a = M$. The black hole (BH) and naked singularity (NS) regions are denoted explicitly. The dotted-dashed curve represents the ergosphere boundaries r_{ϵ}^{\pm} .

$Q^2 < M^2$		$M^2 < Q^2 < (9/8)M^2$	$(9/8)M^2 \leq Q^2 < 3M^2$	$Q^2 \geq 3M^2$
$0 < a \leq a_s$	$a > a_s$	$a > 0$	$a > 0$	$a > 0$
B-H	NS-(IV)	NS-(III)	NS-(II)	NS-(I)
(I) (II)	(I) (II) (IV)	(I) (II) (III) (IV) (*)	(I) (II) (III) (IV)	(I) (II) (III)

FIG. 24: Classification of KN compact object according to the charge-to-mass ratio Q/M and the spin a/M of the source. Black holes can have regions of type **I** and **II** and only naked singularities can accommodate regions of all four types. The type NS-III (with *) has two forbidden orbital regions while NS-II has only one forbidden orbital region.

Another interesting result is that only naked singularities allow orbiting test particles of the type **III** and **IV**, i.e., counter-rotating particles with $L = -L_{\pm}$. Since black holes can have counter-rotating particles only with $L = -L_{+}$, it follows that the presence of counter-rotating particles with $L = -L_{-}$ would necessarily imply the existence of KN naked singularities.

In the case of black holes, we have shown that there exists only one stability region for circular orbits whereas naked singularities present two stability regions separated by one zone of instability. This peculiar structure suggests the possibility of distinguishing black holes from naked singularities by investigating the structure of accretion disks

around the central source. Indeed, if we imagine an idealized accretion disk made of test particles which are moving along circular orbits on the equatorial plane of a KN spacetime, then in the case of a black hole the accretion disk is continuous whereas in the case of a naked singularity it is discontinuous. It would be interesting to find out if this difference will remain in the case of more realistic accretion disks [26–32], and if it could lead to observable effects. This question was also recently analyzed in [33].

During the past few years, much effort has been made to understand the question about the formation of naked singularities [34–36], and about the properties of solutions that describe the gravitational field of such hypothetical compact objects [37–44]. The present work contributes to this discussion in the sense that it shows the possibility of identifying KN naked singularities by investigating the properties of their accretion disks.

However, there are indications that the rigid structure of the KN solution is not adequate to correctly describe naked singularities. In fact, several studies show that KN singularities are highly unstable configurations [45, 46] that, therefore, cannot exist in Nature. Nevertheless, it is important to emphasize that the stability problem of the KN solution is still a subject under debate. For instance, in [58] the slow-rotation limit of the KN black holes has been addressed recently by using gravito-electromagnetic perturbations. Using a self-consistent calculation of scalar, electromagnetic and gravitational quasi normal modes up to linear order in the spin and arbitrary values of the charge, a fully-consistent stability analysis of the KN is provided. Since none of these modes is unstable, the authors suggest that their calculation provides solid (numerical) evidence for the stability of the KN metric in the non extremal regime, an analysis that, in principle, could be generalized to the naked singularity regime. We conclude that it is important to continue the study of the stability of the KN spacetime. It is also possible to consider more general solutions that generalize the KN spacetime and could describe the gravitational field of compact objects. The first possibility is to consider solutions with quadrupole and higher moments [47]. Since already in the case of a static field with only quadrupole moment, there are many possible solutions [48–54] and most of them are quite difficult to handle, we propose to use the recently proposed reinterpretation of the Zipoy-Voorhees [55–57] solution which from the mathematical point of view is the simplest generalization of the Schwarzschild black hole solution with a quadrupole moment. Nevertheless, to understand properly the main features of the solutions with quadrupole it is important to address the limiting cases of the exact KN metric. We expect to investigate this problem in the near future.

Acknowledgments

One of us (DP) gratefully acknowledges financial support from the Blanceflor Boncompagni-Ludovisi née Bildt Foundation. This work was also supported by A. Della Riccia Foundation. This work was supported by CONACyT-Mexico, Grant No. 166391, by DGAPA-UNAM, and by CNPq-Brazil.

Appendix A: Limiting cases

To study circular motion in the gravitational field described by the KN spacetime, in Sec. II A we introduced the spin parameters a_i , a_T and \tilde{a}_\pm which determine the boundaries of the regions where circular motion is allowed for both black holes and naked singularities. When these parameters coincide, the extended regions allow only a limited number of orbits which depend on the charge-to-mass ratio of the central source. In this Appendix, we present the characteristics of these limiting orbits.

First, orbits with $\tilde{a}_+ = \tilde{a}_-$ are characterized by the radii

$$r_\epsilon \equiv Q^2/2M = r_*/2, \quad r_{y_1} \equiv \frac{1}{3M} \left(M^2 + Q^2 + 2\bar{y} \cos \left[\frac{1}{3} \arccos \left(\frac{\hat{y}}{8\bar{y}^3} \right) \right] \right), \quad (\text{A1})$$

$$r_{y_2} \equiv \frac{1}{3M} \left[M^2 + Q^2 - 2\bar{y} \sin \left(\frac{1}{6} \left[\pi + 2 \arccos \left(\frac{\hat{y}}{8\bar{y}^3} \right) \right] \right) \right], \quad (\text{A2})$$

$$r_{y_3} \equiv \frac{1}{3M} \left(M^2 + Q^2 - 2\bar{y} \sin \left[\frac{1}{3} \arcsin \left(\frac{\hat{y}}{8\bar{y}^3} \right) \right] \right), \quad (\text{A3})$$

$$\bar{r}_{y_1} \equiv \frac{1}{3M} \left(M^2 + Q^2 + \hat{y}^{1/3} \right), \quad \bar{r}_{y_2} \equiv \frac{1}{6M} \left(2M^2 + 2Q^2 - \hat{y}^{1/3} \right), \quad (\text{A4})$$

$$\bar{r}_{y_3} \equiv \frac{1}{6M} \left(2M^2 + 2Q^2 + \left(\hat{y} - 3\sqrt{3}\sqrt{Q^6(8 - 13Q^2 + 16Q^4)} \right)^{1/3} \right) \quad (\text{A5})$$

$$+ \left(\hat{y} + 3\sqrt{3}\sqrt{Q^6(8 - 13Q^2 + 16Q^4)} \right)^{1/3}, \quad (\text{A6})$$

with $\bar{y} \equiv \sqrt{M^4 - M^2Q^2 + Q^4}$, and $\hat{y} \equiv 8M^6 - 12M^4Q^2 + 15M^2Q^4 + 8Q^6$. The behavior of these radii is illustrated in Fig. 25.

Moreover, for the limiting case $a_i = a_T$ we obtain the following radii

$$r_\pi = \frac{4Q^2}{3M^2}, \quad r_p^\pm \equiv \frac{1}{3M} \left(9M^2 - 4Q^2 \pm 2Q\sqrt{9M^2 - 8Q^2} \right). \quad (\text{A7})$$

Finally, the condition $a_i = \tilde{a}_-$ leads to the orbits characterized by the radii

$$r_\phi \equiv \frac{1}{2} \left(\sqrt{9M^2 + 8Q^2} - 3M \right), \quad (\text{A8})$$

$$r_{\rho_\pm}/M \equiv \frac{1}{6} \left(9 - \sqrt{3}v \pm \frac{\sqrt{3}}{2M} \sqrt{-4(v^2M^2 + 45M^2 + 12Q^2) - \frac{96\sqrt{3}(5Q^2 - 9M^2)}{v}} \right), \quad (\text{A9})$$

$$\bar{r}_{\rho_\pm}/M \equiv \frac{1}{6} \left(9 + \sqrt{3}v \pm \frac{\sqrt{3}}{2M} \sqrt{-4(v^2M^2 + 45M^2 + 12Q^2) + \frac{96\sqrt{3}(5Q^2 - 9M^2)}{v}} \right), \quad (\text{A10})$$

$$(\text{A11})$$

where

$$\zeta \equiv (9261M^6 - 12096M^4Q^2 + 5814M^2Q^4 - 568Q^6 + 6\sqrt{3}Q^2\sqrt{5292M^8 + 65340M^6Q^2 - 91881M^4Q^4 + 45512M^2Q^6 - 6272Q^8})^{1/3}, \quad (\text{A12})$$

and $v \equiv \sqrt{\frac{441M^6 + 100M^2Q^4 - 15M^3\zeta + \zeta^2 - 4MQ^2(96M^3 + \zeta)}{M^3\zeta}}$.

In Fig. 25, we show the behavior of the orbits in terms of the ratio Q/M . In Fig. 25-left, we consider the first set of orbits $\{r_*/2, r_*, r_\pi, \bar{r}_{y_1}, \bar{r}_{y_2}, \bar{r}_{y_3}\}$. These radii exist for all values of Q/M ; they decrease when Q/M decreases and diverge for as Q/M increases. This means that the ranges where these radii have boundaries become larger as Q/M increases. The situation is completely different for the radii of the second set, $\{r_{\rho_\pm}, \bar{r}_{\rho_\pm}, r_\phi, r_p^\pm\}$, plotted in Fig. 25(b). These orbits determine a closed region of the space $r \times Q$. The radii r_p^\pm , where $a_i = a_T$, and $(r_{\rho_\pm}, \bar{r}_{\rho_\pm})$, where $a_i = \tilde{a}_-$, are defined for a closed range of values of Q/M and are bounded. The distance between these two radii can become null and has a maximum as a function of the charge.

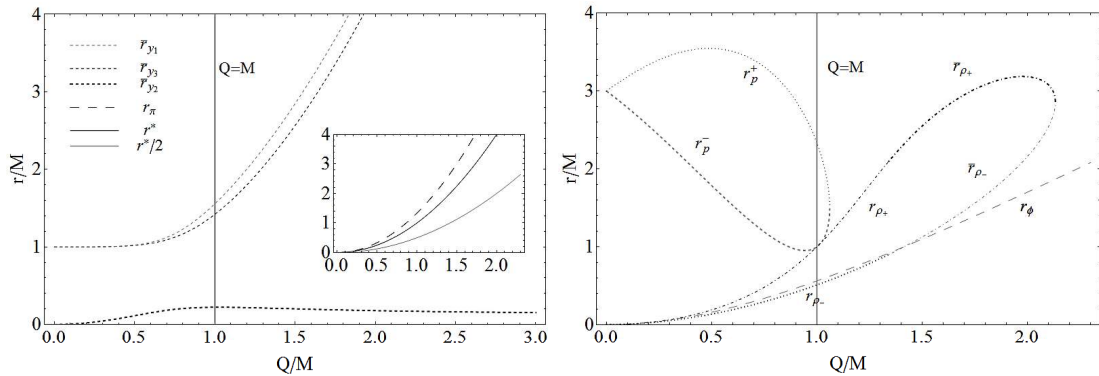


FIG. 25: Left: Plot of $r_*/2$, r_* , r_π , \bar{r}_{y_1} , \bar{r}_{y_2} and \bar{r}_{y_3} as functions of Q/M . Right: Plot of r_{ρ_\pm} , \bar{r}_{ρ_\pm} , r_ϕ and r_p^\pm as functions of Q/M .

Appendix B: Naked singularities with $Q < M$

In Sec. IV A, we use the expressions for the spin $a_1 \equiv a_-$ and $a_2 \equiv a_+$ with

$$a_{\pm} \equiv \sqrt{\left(\frac{27}{64} + 2Q^2 - \frac{3Q^4}{4} + \frac{1}{2}\sqrt{\frac{\iota_3}{768} 2^{1/3} + \iota_4} \pm \frac{\sqrt{\iota_5}}{32\sqrt{6}}\right)}, \quad (\text{B1})$$

in the study of solutions of the equations of motion with $L = 0$, where

$$\begin{aligned} \iota_5 \equiv & 3(27 + 128Q^2 - 48Q^4)^2 - 192Q^2(144 - 81Q^2 + 92Q^4 + 32Q^6) - \\ & \frac{2592 \cdot 2^{1/3} Q^4 (9216 - 10368Q^2 + 15529Q^4 + 2496Q^6 + 5232Q^8 + 2560Q^{10})}{\iota_3} - 2^{2/3} \iota_3 + \\ & \frac{3(19683 - 93312Q^2 - 337392Q^4 + 2522240Q^6 - 3866496Q^8 + 780288Q^{10} + 4096Q^{12})}{\sqrt{\frac{2}{3} 2^{2/3} \iota_3 + 1024\iota_4}}; \end{aligned} \quad (\text{B2})$$

$$\begin{aligned} \iota_4 \equiv & \frac{1}{1024\iota_3} \left[1728 \cdot 2^{1/3} Q^4 (9216 - 10368Q^2 + 15529Q^4 + 2496Q^6 + 5232Q^8 + 2560Q^{10}) + \right. \\ & \left. (729 + 32Q^2(-72 + 593Q^2 - 568Q^4 + 8Q^6)) \iota_3 \right]; \end{aligned} \quad (\text{B3})$$

$$\iota_3 \equiv (\iota_2 + \sqrt{(\iota_1)})^{1/3} \quad (\text{B4})$$

$$\begin{aligned} \iota_2 \equiv & 93312Q^6(884736 - 1492992Q^2 + 2656080Q^4 - 819693Q^6 + 1183756Q^8 + 426790Q^{10} + \\ & + 924864Q^{12} + 33280Q^{14} + 65536Q^{16}); \end{aligned} \quad (\text{B5})$$

$$\iota_1 \equiv 34828517376Q^{20}(10 - 37Q^2 + 16Q^4)^3(8 - 13Q^2 + 16Q^4)(783 + 311Q^2 + 128Q^4)^2. \quad (\text{B6})$$

To facilitate the presentation we use in the above formulas the normalized quantities $Q \rightarrow Q/M$ and $r \rightarrow r/M$. The behavior of the spin parameters is depicted in Fig. 26. These parameters were used in Table V to determine

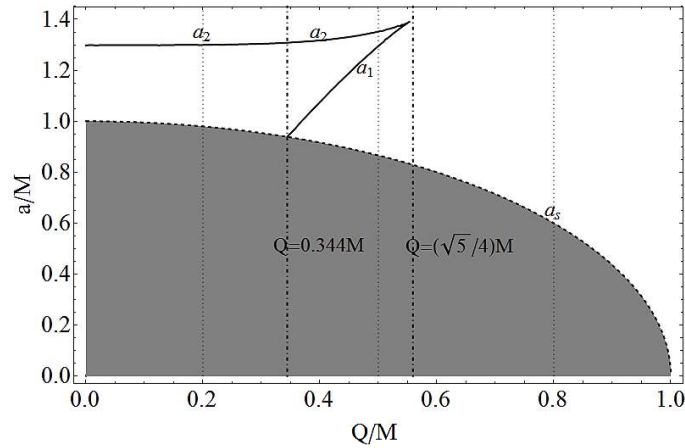


FIG. 26: Circular orbits in Kerr–Newman naked singularity for $Q < M$ are explored. We plot the parameters a_1, a_2 and a_0 as functions of the charge Q/M .

the existence regions for solutions with $L = 0$. As discussed in Sec. IV A, it is important to consider in particular the ranges $Q/M \in]0, 0.344263]$ with (a_1, a_s) , $Q/M \in]0.344263, \sqrt{5}/4[$ with (a_1, a_2, a_s) , and $Q/M \in [\sqrt{5}/4, 1]$ with a_s only.

[1] J. Bičák, C. Hoenselaers, Phys. Rev. D **31**, 10, 24762479 (1985).

- [2] A. Saa and R. Santarelli, *Phys. Rev. D* **84** 027501 (2011).
- [3] C. A. López, *Nuovo Cimento B*, **11**, 76 B, 9-27 (1983).
- [4] C. Bambi and G. Lukes-Gerakopoulos, arXiv:1302.0565 [gr-qc].
- [5] A. Wunsch, T. Müller, D. Weiskopf and G. Wunner, *Phys. Rev. D* **87** 024007 (2013).
- [6] D. Pugliese, H. Quevedo and R. Ruffini, *Phys. Rev. D* **83**, 024021 (2011).
- [7] D. Pugliese, H. Quevedo and R. Ruffini, *Phys. Rev. D* **84** 044030 (2011).
- [8] D. Pugliese, H. Quevedo and R. Ruffini, *Phys. Rev. D* **83** 104052 (2011).
- [9] C. W. Misner, K. S. Thorne, & J. A. Wheeler, *Gravitation*, W. H. Freeman, 1973.
- [10] Z. Stuchlik, *Astronomical Institutes of Czechoslovakia, Bulletin*, **31**, 3, 129-144, (1980).
- [11] J. Bik, Z. Stuchlik, and V. Balek, *Bull. Astronom. Inst. Czechoslovakia*, **40**(2), 6592, (1989).
- [12] V. Balek, J. Bicak, Z. Stuchlik, *Astronomical Institutes of Czechoslovakia, Bulletin (ISSN 0004-6248)*, **40**, 3, 133-165, (1989).
- [13] J. Kovar, O. Kopacek, V. Karas and Z. Stuchlik, *Class. Quant. Grav.* **27** 135006 (2010).
- [14] J. Kovar, Z. Stuchlik and V. Karas, *Class. Quant. Grav.* **25** 095011 (2008).
- [15] Z. Stuchlik and S. Hledik, *Class. Quantum Grav.* **17**, 21, 4541, (2000).
- [16] J. L. Cindra, *Class. Quantum Grav.* **6**, 857, (1989).
- [17] Z. Stuchlik, *Astronomical Institutes of Czechoslovakia, Bulletin*, **32**, 6, 366-373, (1981).
- [18] R. Bekgamini, G. Denaedo, A. Treves *Lettere al Nuovo Cimento*, **11**, 3, 183-186, (1974).
- [19] N. K. Rajesh, C. V. Vishveshwara, *Class. Quantum Grav.* **13** (7), 1783-1795, (1996).
- [20] Z. Stuchlik, S. Hledik and J. Jurn, *Class. Quantum Grav.* **17**, 14 2691, (2000).
- [21] J. Kovar, O. Kopacek, V. Karas and Y. Kojima, *Class. Quant. Grav.* **30** 025010 (2013).
- [22] M. A. Abramowicz, J. C. Miller, Z. Stuchlik, *Phys. Rev. D* **47**, 14401447 (1993).
- [23] A. Burinskii, *Grav. Cosmol.* **14** 109 (2008).
- [24] H. I. Arcos and J. G. Pereira, *Gen. Rel. Grav.* **36** 2441 (2004).
- [25] F. de Felice, *Astronomy and Astrophysics*, **34**, 15 (1974).
- [26] E. Babichev, S. Chernov, V. Dokuchaev and Y. Eroshenko, *Phys. Rev. D* **78** 104027 (2008).
- [27] Z. Stuchlik, J. Bicak, V. Balek, *Gen. Rel. Grav.*, **31**, 1, 53-71 (1999).
- [28] Z. Stuchlik, J. Jurn, *Physical Processes in Interacting Binaries*, proceedings of the 19th Stellar Conference of the Slovak and Czech Astronomical Institutes, 7th-9th November 1996, Tatranska Lomnica, Slovakia. Edited by D. Chochol, A. Skopal, T. Pribulla. *Astronomical Institute of the Slovak Academy of Sciences*, 115, (1996).
- [29] Z. Stuchlik, S. Hledik, *Acta Phys. Slovaca*, **48**, 5, 549-562, (1998).
- [30] J. Kovr, Z. Stuchlik, V. Karas, *Proceedings of RAGtime 8/9 2006/2007*, Hradec nad Moravic, Opava, Czech Republic, S. Hledik and Z. Stuchlik, editors, *Silesian University in Opava*, 125-138, (2007).
- [31] E. P. Esteban, N. Marrero. *Il Nuovo Cimento B*, **11**, 105, 6, 647-656, (1990).
- [32] M. Jaroszynski, M. A. Abramowicz, B. Paczynski, *Acta Astronomica*, **30**, 1, 1-34, (1980).
- [33] Z. Kovacs and T. Harko, *Phys. Rev. D* **82** 124047 (2010).
- [34] M. Patil, P. S. Joshi, *Phys. Rev. D* **82** 104049 (2010).
- [35] P. S. Joshi and D. Malafarina, *Int. J. Mod. Phys. D* **20** 2641 (2011).
- [36] M. Patil, P. S. Joshi, M. Kimura and K. -i. Nakao, *Phys. Rev. D* **86** 084023 (2012).
- [37] J. M. Cohen, R. Gautreau, *Phys. Rev. D* **19**, 8, (1979).
- [38] R. Di Criscienzo, L. Vanzo and S. Zerbini, *JHEP* **1005** 092 (2010).
- [39] E.P.T. Liang, *Phys. Rev. D*, **9**, 12, (1974).
- [40] G. Dotti and R. J. Gleiser, *Class. Quant. Grav.* **26** 215002 (2009).
- [41] R. Casadio, S. Fabi and B. Harms, *Phys. Rev. D* **70** 044026 (2004).
- [42] G. Z. Toth, *Gen. Rel. Grav.* **44**2019 (2012).
- [43] K. S. Virbhadra and C. R. Keeton, *Phys. Rev. D* **77** 124014 (2008).
- [44] K. S. Virbhadra and G. F. R. Ellis, *Phys. Rev. D* **65** 103004 (2002).
- [45] G. Dotti, R. J. Gleiser, I. F. Ranea-Sandoval and H. Vucetich, *Class. Quant. Grav.* **25** 245012 (2008).
- [46] P. Pani, E. Barausse, E. Berti and V. Cardoso, *Phys. Rev. D* **82**, 044009 (2010).
- [47] H. Quevedo, *Fort. Phys.* **38**, 733 (1990).
- [48] H. Weyl, *Ann. Phys.* **54**, 117 (1917).
- [49] J. Chazy, *Bull. Soc. Math. France* **52** 17 (1924).
- [50] H. Curzon, *Proc. London Math. Soc.* **23**, 477 (1924).
- [51] G. Erez and N. Rosen, *Bull. Res. Council of Israel* **8F**, 47 (1959).
- [52] Ts. I. Gutsunaev and V. S. Manko, *Gen. Rel. Grav.* **17**, 1025 (1985).
- [53] H. Quevedo, *Gen. Rel. Grav.* **19**, 1013 (1987).
- [54] H. Stephani, D. Kramer, M. A. H. MacCallum, C. Hoenselaers, and E. Herlt, *Exact Solutions of Einstein's Field Equations* (Cambridge University Press, Cambridge, UK, 2003).
- [55] D. M. Zipoy, *J. Math. Phys.* **7**, 1137 (1966).
- [56] B. Voorhees, *Phys. Rev. D* **2**, 2119 (1970).
- [57] H. Quevedo, *Int. J. Mod. Phys. D* **20** 1779 (2011).
- [58] P. Pani, E. Berti and L. Gualtieri, *Gravito-Electromagnetic Perturbations of Kerr-Newman Black Holes: Stability and Isospectrality in the Slow-Rotation Limit*, arXiv:1304.1160 [gr-qc].